J. Fluid Mech. (1993), *vol.* 250, *pp.* 385–421

Surface motion induced by the interaction of pulsed laser radiation with highly absorbing dielectric fluids

By KONSTANTIN A. NAUGOL'NYKH, OLEG V. PUCHENKOV, VICTOR V. ZOSIMOV AND ALEXANDER E. PASHIN

N. N. Andreev Acoustics Institute, 117036 Moscow, Russia

(Received 24 July 1992 and in revised form 28 October 1992)

The disturbances on the free surface of dielectric fluids resulting from intense laser heating of their boundary layer are studied theoretically and experimentally. The heating is accompanied by pronounced evaporation from the surface and thereby leads to a recoil pressure momentum applied to the surface. For small values of total momentum transferred to the fluid, the low-amplitude initially hollow-like displacement of the surface in the impact zone decays to produce linear gravity–capillary waves (GCW) spreading out on the surface. This regime is treated analytically and the results obtained are compared with experiments involving weakly viscous (water, ethanol) and highly viscous (glycerol) liquids. An experimental arrangement for remote generation and subsequent detection of probe GCW-packets is given. The evolution of broadband GCW-disturbances on clean and surfactant-contaminated water surfaces are described. Results of GCW-attenuation spectrum measurements on clean water surfaces and on film-covered surfaces are presented.

High total recoil momentum values give rise to substantially nonlinear surface motion: after a short transient stage the surface takes the shape of a hemisphere expanding into the liquid, and later the liquid above the hemisphere closes up to form a cavity and slow down the expansion. For this regime the dynamics of the hemisphere expansion are determined and satisfactory agreement with experimental data obtained with the shadowgraph technique is established. Consistency of theory and experiment allowed the determination of the total recoil pressure momentum and its surface distribution.

In the intermediate case of moderate values of recoil momentum, the nonlinear evolution of broadband GCW-packets on clean and surfactant-contaminated water surfaces is investigated experimentally.

1. Introduction

The study of fluid motion induced by an impact on its surface started almost a century ago when Worthington & Cole (1897) examined by means of single-flash photography the process of balls dropping onto fluids. Later, results of many experiments and numerical simulations of the phenomenon were published. A comprehensive list of references is given in the recent work of Oguz & Prosperetti (1990). Analogous phenomena were found when investigating the interaction of high-power pulsed laser radiation with highly absorbing liquids. Initially, Emmony, Geerken & Straaijer (1976) recorded the interaction of a CO_2-laser pulse with a free

liquid surface by high-speed photography. They observed a vapour cloud ejected above the surface and a gas bubble generated below the surface that expanded into the liquid. The initiation and growth of the bubble were, however, erroneously attributed to the cavitation induced by the shock wave propagating away from the surface. Noteworthy is the fact that for a long time after this work, attention was primarily concentrated on the registration and analysis of elastic disturbances, i.e. shock waves in air and short high-amplitude ultrasonic pulses in a fluid (the studies of Bell & McCabee 1974, Bunkin & Tribel'skii 1980 and Emmony 1985 are relevant for the reader wishing to get acquainted with successive developments of the problem).

The theoretical treatment of laser light interaction with highly absorbing fluids is rather difficult, and in spite of numerous experiments is far from completion. The acoustodiagnostic technique alone (used, for example, by Alekseev *et al.* 1987) was found not to provide comprehensive information about the interaction. Therefore, the idea of also examining the 'hydrodynamic stage' of the fluid disturbances was suggested. Zosimov *et al.* (1989) have shown that under real experimental conditions laser-induced fluid surface displacements may be calculated by solving the initial value problem for incompressible fluid flow initiated by a given velocity potential distribution on the free surface. The theory proposed and preliminary experiments have led an explanation of the motion observed by the recoil pressure impact on the surface. An initially hemispheric shape displacement evolves to produce a closed bubble below the surface in the manner illustrated in figure 4. To some extent the phenomenon is similar to the well-known boundary point explosion problem considered, for example, theoretically and experimentally by Deribas & Pohozhaev (1962) and experimentally by Minin (1964).

A remarkable peculiarity of the 'laser blast' is the larger variety of possible disturbances (down to small, linear surface displacements) that is obviously accounted for by the adjustable value and configuration of recoil momentum transferred to the fluid. Furthermore, in this case the motion induced may be virtually completely treated analytically without the need for a bulky and somewhat unclear numerical simulation, e.g. by the boundary elements method. So, provided the initial impact value is small enough, the free surface axially symmetric motion may be calculated exactly. The analogous initial problem for gravity–capillary wave (GCW) induced by δ-functional point impact was considered by Lamb (1932) for an inviscid fluid. Recently Le Mehaute (1988) has used Lamb's calculations to describe gravity–capillary rings generated by water drops. But a sad mistake in the dimensionless derivation led the author to an erroneous integral expression for surface displacement (expression (17) on p. 418 of Le Mehaute (1988) is obviously divergent) and thereby to irrelevant conclusions. In the present study Lamb's theory is generalized to cover the case of viscous fluids with a film-covered surface. This made it possible to develop a new remote mode method of diagnostics of fluid–air interface properties, tested experimentally for the first time by Puchenkov & Pashin (1989) and considered by Egerev, Lyamshev & Puchenkov (1990) among the possible dynamic diagnostic techniques.

The remote mode of generation and detection of predetermined GCW trains turned out to be convenient for the investigation of the nonlinear evolution of wideband surface wavetrains because of the easy control of amplitude/shape characteristics of GCWs generated by a 'laser blast'.

2. Problem formulation

Fluid surface disturbances resulting from the interaction of pulsed laser radiation with highly absorbing dielectric liquids are considered. For small laser energies heat release leads to stress wave generation in a fluid (the so-called 'photoacoustic effect'). The features of the phenomenon are now well enough established (for details the recent review of Egerev *et al.* 1990 may be recommended). Surface disturbances in this case are negligible. As Kolomenskii (1986) estimated, vertical displacement induced by optical radiation of intensity $I = 10\ \mathrm{W/cm^2}$ is equal to approximately 10^{-7} cm. At higher energies of laser radiation intense evaporation in the boundary layer of the fluid is developed. And above a certain threshold value optical breakdown in the vapour cloud near the surface occurs. Physical aspects of the phenomenon are considered by Bunkin & Tribel'skii (1980), Alekseev *et al.* (1987) and others. Here just a general outline is given. Hot vapour ejection from the surface during laser heating results in recoil pressure momentum applied to the fluid. The pressure impact generates sharp powerful ultrasonic transients in the bulk of the fluid and displacements of its surface. The measurements taken by many investigators revealed that for typical experimental conditions the pressure on the water surface lies in the range 1–300 atm (see Alekseev *et al.* 1987). Noteworthy is the fact that there are three successive stages of the interaction dynamics.

First, an 'ablation' stage, when evaporation leads to the generation of a shock wave in air and ultrasonic transients in the fluid. The duration of this stage virtually coincides with the time-width of the laser pulse and for the most frequently used CO_2-laser is approximately equal to 10 μs. Thereafter the pressure in the interaction zone rapidly decreases and the recoil pressure momentum transferred to the liquid gives rise to incompressible flow formation in the fluid halfspace. In other words, the action of a short pressure pulse on a fluid surface induces an initial velocity distribution in the fluid without appreciable displacements (Batchelor 1967). Acoustic pulse propagation has to be considered as a finite-time (taking into account fluid compressibility) process of this distribution formation. The second stage of interaction dynamics is the initial displacement of the liquid surface in the region of pressure impact. Finally, in the 'ripples' stage, this initial disturbance decays into GCWs spreading out axially on the surface.

Successive stages of the phenomena arising from the interaction of powerful laser radiation with a liquid are represented schematically in figure 1. Characteristic time periods of the development of disturbances marked in figure 1 are relevant for the case under consideration in the present study when the size of the impact spot on the surface is about a few millimeters.

As follows from figure 1, the ablation stage is quite short compared to the displacement and ripples stages. Therefore, it seems to be pertinent to regard the pressure impact as instantaneous and to treat the problem of the determination of surface disturbances as an initial value problem. The accurate derivation of conditions validating the assumption stated is given below.

We have to evaluate the order of the terms in the Navier–Stokes equation for the boundary layer:

$$\frac{\partial \boldsymbol{v}}{\partial t} + (\boldsymbol{v}\cdot\nabla)\,\boldsymbol{v} = -\frac{\nabla p}{\rho} + \nu\Delta\boldsymbol{v}, \tag{1}$$

where ρ is the density of fluid, p is the excess pressure induced by the action of recoil momentum, $\boldsymbol{v}$ is the flow velocity and ν is the kinematic viscosity. We shall further consider the case of incompressible liquid $\rho = \rho_0 = \text{const}$, which implies $p \ll \rho_0 c^2$ (c is

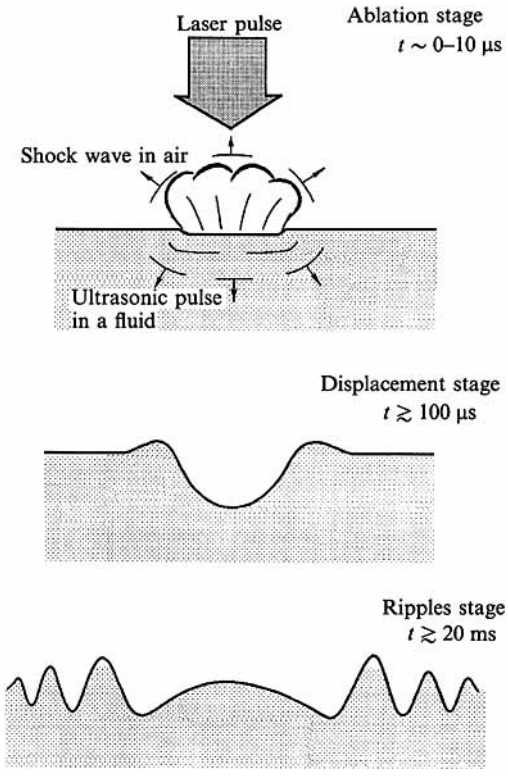

FIGURE 1. Schematic drawing of phenomena following the interaction of laser radiation with a liquid.

the sound velocity). For water $\rho_0 c^2 \approx 2.2 \times 10^9$ Pa while the laser evaporation-driven pressure is always below 10^8 Pa. On the fluid surface the pressure increment p is equal to the pulsed recoil pressure P_s. It is convenient to introduce the total momentum transferred to the surface Λ and its average surface density Π_{av}:

$$\Lambda = \iint P_s(t, \boldsymbol{R})\, \mathrm{d}t\, \mathrm{d}^2\boldsymbol{R}, \quad \Pi_{av} = \frac{\Lambda}{\pi a^2}$$

(a is the characteristic impact spot size. $\boldsymbol{R}$ is the radius vector in the boundary plane). It is the dimension of a that gives the scale to estimate the values of spatial derivatives in (1). In the linear approximation the velocity component normal to the surface v_z is evaluated by

$$v_z \approx \frac{\Pi_{av}}{\rho_0 a(1 + \nu\tau/a^2)}$$

and the surface displacement h at the end of the action of the recoil pressure, at a time $t = \tau$, is given by

$$h \approx \frac{\tau}{\rho_0 a} \frac{\Pi_{av}}{(1 + \nu\tau/a^2)}. \tag{2}$$

The fluid surface may be regarded as undisturbed at the end of recoil momentum impact in the case of $h \ll a$ or, by substituting (2) for h,

$$\Pi_{av} \ll (\rho_0/a^2\tau)[1 + \nu\tau/a^2]. \tag{3}$$

The linear estimation for v_z enables us to determine the order of the nonlinear term in (1). Bearing in mind the continuity equation for incompressible liquid and the boundary conditions on a free liquid surface, we may write the relation of the two terms on the left-hand side of (1) as approximately

$$\frac{(\boldsymbol{v}\cdot\boldsymbol{\nabla})v}{\partial v/\partial t} \approx \frac{\tau v_z}{a} \approx \frac{\tau \Pi_{\mathrm{av}}}{\rho_0 a^2(1+\nu\tau/a^2)}.$$

It is clear that the nonlinear term can be neglected when condition (3) is valid. To realize the essence of (3) let us consider the common case of water irradiation by a TEA CO_2-laser pulse. The typical parameters are $\tau = 10\ \mu\mathrm{s}$, $\rho_0 = 10^3\ \mathrm{kg/m^3}$, and taking $a = 2\ \mathrm{mm}$ one obtains the limitation: $\Pi_{\mathrm{av}} \ll 400\ \mathrm{Pa\cdot s}$. This is a fairly reasonable estimation if we take into account that peak pressure measurements in various experiments exhibit maximum values of 100–200 atm when the laser intensity is below the optical breakdown threshold: $I \ll 4\times 10^7\ \mathrm{W/cm^2}$ (see Alekseev *et al.* 1987 and references therein). Note that taking of viscosity into account gives a virtually negligible correction. Even for such a viscous fluid as glycerol ($\nu = 8\times 10^{-4}\ \mathrm{m^2/s}$ at 24 °C) the second term in the square brackets of (3) is equal to approximately 2×10^{-3} for the parameters listed above. This is quite natural in view of the small timescale of the initial stage of the phenomenon in question.

Thus, condition (3) makes it possible to reduce the problem of determination of liquid surface motion induced by the action of intense laser radiation to the examination of incompressible flow generated by a given initial distribution of recoil momentum on the free liquid surface. An analytical solution to the problem is given in the next section.

3. Surface displacements in the impact region

3.1. *Theoretical model; linear approximation*

In the general case, the flow originating from the initial pressure impact can be determined only by numerical simulation methods which are analogous to those described by Dommermuth & Yue (1987). At the same time the principal features of the flow may be developed on the basis of analytical models that correspond to some experimentally realizable conditions and give a consistent explanation of the phenomena.

Let us first examine the linear case of small surface disturbance from equilibrium: $h(\boldsymbol{R}, t) \ll a$. To find the physical consequences of this approximation we shall determine the energy balance corresponding to the surface motion. The total initial (kinetic) energy of the flow by the end of impact T_{in} may be deduced, neglecting viscosity due to the rapidity of the evaporation process. The corresponding surface integral is

$$T_{\mathrm{in}} = \tfrac{1}{2}\rho_0 \int \phi \frac{\partial \phi}{\partial n}\,\mathrm{d}S, \tag{4}$$

where ϕ is the velocity potential, and $\partial\phi/\partial n$ is the derivative along the outward normal to the surface, i.e. along the $\mathrm{d}\boldsymbol{S}$ direction. Using the estimation for v_z and the value of Π_{av} introduced in the previous section, one can evaluate the flow energy as follows:

$$T_{\mathrm{in}} \approx a\Pi_{\mathrm{av}}^2/\rho_0. \tag{5}$$

This energy is eventually transformed into the energy of deformation of the initially plane liquid surface and into viscous dissipation energy (the variation of potential

energy in the gravity field is negligible for small values of a). For the case of surface deformation into a hemisphere of radius a, the linear approximation implies that the energy T_{in} is much smaller than the energy expended during such a deformation. The energy of surface deformation ΔE_{srf} is proportional to the difference of initial and final surface area: $\Delta E_{\text{srf}} \approx \sigma \pi a^2$ (σ is the surface tension) and the dissipation losses per unit time are given by the expression (Landau & Lifshitz 1986, §16):

$$\frac{\partial T}{\partial t} = -\nu \rho_0 \int \nabla(v^2)\, \mathrm{d}S, \tag{6}$$

where integration is performed over the liquid surface, the element $\mathrm{d}S$ being oriented along the outward normal. The total amount of energy dissipated during the deformation ΔE_{loss} is evaluated by the expression

$$\Delta E_{\text{loss}} \approx \pi a^2 \nu \rho_0 v_z \approx \nu \Pi_{\text{av}} a.$$

So, the linear approximation is valid only when the following inequality holds:

$$\Pi_{\text{av}} \ll \max\left((a\sigma\rho_0)^{\frac{1}{2}}, \rho_0 \nu\right). \tag{7}$$

For inviscid fluids such as water the first condition actually limits the Π_{av} value, which implies that most of the kinetic energy is expended on surface deformation and the smaller remainder is dissipated. For highly viscous fluids such as glycerol the two conditions (7) give the same order of magnitude for Π_{av}.

We shall further suggest that the $\Pi(R)$ distribution is axially symmetric: $\Pi(R) = \Pi(r)$, hence disturbances arising should be axially symmetrical, as well. Linearized hydrodynamic equation and boundary conditions adopted in the theoretical linear approximation model would appear to be useful written in cylindrical coordinates. The complete system of equations comprises the linearized Navier–Stokes equation:

$$\frac{\partial v_r}{\partial t} = -\frac{1}{\rho_0}\frac{\partial p}{\partial r} + \nu\left(\Delta v_r - \frac{v_r}{r^2}\right), \tag{8a}$$

$$\frac{\partial v_z}{\partial t} = -\frac{1}{\rho_0}\frac{\partial p}{\partial z} + \nu \Delta v_z \tag{8b}$$

(here v_r and v_z denote velocity components in the boundary plane and in the perpendicular direction, respectively; $\boldsymbol{v} = (v_r, v_z)$; p is the pressure increment, the continuity equation for an incompressible liquid:

$$\frac{1}{r}\frac{\partial (r v_r)}{\partial r} + \frac{\partial v_z}{\partial z} = 0, \tag{9}$$

and also two linearized boundary conditions for the undisturbed surface of the fluid at $z = 0$:

$$p - \sigma_0 \frac{1}{r}\frac{\partial}{\partial r}\left(r\frac{\partial h}{\partial r}\right) + \rho_0 g h - 2\eta \frac{\partial v_z}{\partial z} = P_{\text{s}}, \tag{10a}$$

$$\frac{\partial \sigma(r)}{\partial r} + \eta\left(\frac{\partial v_r}{\partial z} + \frac{\partial v_z}{\partial r}\right) = 0, \quad \frac{\partial h}{\partial t} = v_z \tag{10b}$$

($\eta = \nu\rho_0$ is the dynamic viscosity, g is the gravitational acceleration). Recording the boundary conditions in the form of (10a,b) we suppose that on the unperturbed surface the coefficient of surface tension σ is constant: $\sigma = \sigma_0$, though it can be

modulated during the surface displacement: $\sigma = \sigma_0 + \sigma(r)$ (for example, in the case of film-covered surfaces). Taking $\sigma(r) \ll \sigma_0$, we neglect the $\sigma(r)$ term in (10*a*). Note also that the case of deep water is considered, which implies appropriate decreasing conditions for $z \to -\infty$.

The system of equations (8)–(10) is solved in standard manner by using Fourier–Bessel and Laplace integral transform techniques. To simplify derivation it is convenient to introduce the stream function ψ in accordance with (9):

$$v_r = \frac{1}{r}\frac{\partial \psi}{\partial z}, \quad v_z = -\frac{1}{r}\frac{\partial \psi}{\partial r}.$$

Then by eliminating p the system (8) is reduced to

$$\left(\frac{\partial}{\partial t} - \nu \mathrm{H}^2\right) \mathrm{H}^2 \psi = 0, \tag{11}$$

where the operator

$$\mathrm{H}^2 = \frac{\partial^2}{\partial z^2} + \frac{\partial^2}{\partial r^2} - \frac{1}{r}\frac{\partial}{\partial r}.$$

The boundary conditions can be rewritten

$$r\frac{\partial \sigma(r)}{\partial r} + \eta\left(\frac{\partial^2 \psi}{\partial z^2} - \frac{\partial^2 \psi}{\partial r^2} + \frac{1}{r}\frac{\partial \psi}{\partial r}\right) = 0, \tag{12a}$$

$$-\sigma_0 \frac{1}{r}\frac{\partial}{\partial r}\left(r\frac{\partial h}{\partial r}\right) + 2\eta \frac{1}{r}\frac{\partial^2 \psi}{\partial z \partial r} + p + \rho_0 g h = P_s, \tag{12b}$$

$$\frac{\partial h}{\partial t} = -\frac{1}{r}\frac{\partial \psi}{\partial r}. \tag{12c}$$

Introducing the pair of integral transforms in the form

$$\hat{\psi}(k, s, z) = \int_{-\infty}^{+\infty} \int_0^{\infty} \psi(r, t, z)\, J_1(kr)\, \mathrm{e}^{-st}\, \mathrm{d}r\, \mathrm{d}t, \tag{13a}$$

$$\psi(r, t, z) = \frac{1}{2\pi \mathrm{i}} \int_{c_0 - \mathrm{i}\infty}^{c_0 + \mathrm{i}\infty} \int_0^{\infty} \hat{\psi}(k, s, z)\, J_1(kr)\, \mathrm{e}^{st}\, \mathrm{d}s\, \mathrm{d}k, \tag{13b}$$

(c_0, the constant in the inverse Laplace transform, is chosen to make the path of integration pass to the right of singularity points of the function $\hat{\psi}(k, s, z)$). For $p(r, t, z)$ and $h(r, t, z)$ the transform is written, as:

$$\{\hat{p}(k, s, z), \hat{h}(k, s, z)\} = \int_{-\infty}^{+\infty} \int_0^{\infty} \{p(r, t, z), h(r, t, z)\}\, r J_0(kr)\, \mathrm{e}^{-st}\, \mathrm{d}r\, \mathrm{d}t, \tag{14}$$

and the inverse transform is analogous to (13).

After substituting (13) and (14) into (11), (12) we obtain

$$(\partial^2/\partial z^2 - k^2)(\partial^2/\partial z^2 - k^2 + \mathrm{i}\omega/\nu)\, \hat{\psi} = 0, \tag{15a}$$

$$\eta(\partial^2/\partial z^2 + k^2)\, \hat{\psi} = \Sigma(k), \tag{15b}$$

$$(k^2 \sigma_0 + \rho_0 g)\, \hat{h} - 2k\eta(\partial \hat{\psi}/\partial z) - \hat{p} = -\hat{P}_s(k, s), \tag{15c}$$

$$\hat{h} = (k/s)\, \hat{\psi}. \tag{15d}$$

The transform of tangential stresses Σ introduced in (15*b*) takes into account the surface tension coefficient modulation $\sigma(r)$ and will be considered in detail below when

analysing the mechanisms resulting in the dependence of σ on r. Till then we shall take $\Sigma(k) = 0$ (clean surface of a homogeneous liquid). The transform of pulsed recoil pressure $\hat{P}_s(k, s)$ in the limit of $s\tau \ll 1$ (for $\tau \ll 10^{-5}$ s this implies $s < 10^5$ s^{-1} which corresponds to the spectral range of disturbances under consideration) equals

$$\hat{P}_s(k, s) = \int_0^\infty \Pi(r)\, r J_0(kr)\, \mathrm{d}r = \hat{\Pi}(k).$$

The solution of system (15) is sought in the form

$$\hat{\psi} = A\, \mathrm{e}^{-kz} + B\, \mathrm{e}^{-mz}, \quad m^2 = k^2 + s/\nu.$$

This expression is substituted into (15) to provide the system of linear equations for the determination of A and B:

$$2\nu k^2 A + (k^2 + m^2)\, \nu B = 0, \tag{16a}$$

$$(2\nu k^2 + s + \Omega^2/s)\, A + (2\nu k m + \Omega^2/s)\, B = \hat{\Pi}(k)/\rho_0. \tag{16b}$$

Here $\Omega^2 = k^3\tilde{\sigma} + gk$, $\tilde{\sigma} = \sigma_0/\rho_0$. The solution of (16), taking into account transform (14), gives the following expression for $h(r, t)$:

$$h(r, t) = \frac{1}{2\pi \mathrm{i}} \int_{c_0 - \mathrm{i}\infty}^{c_0 + \mathrm{i}\infty} \int_0^\infty \frac{k^2}{\rho_0} \frac{\hat{\Pi}(k)}{\det(k, s)} J_0(kr)\, \mathrm{e}^{st}\, \mathrm{d}s\, \mathrm{d}k, \tag{17}$$

where the determinant of (15) is denoted as $\det(k, s)$. The integral with respect to s is calculated by determining the poles of the integrand from the equation $\det(k, s) = 0$. Most liquids are weakly viscous, so the relation $\nu k^2/s \ll 1$ is valid (the opposite case will be considered below). In this approximation the pole points are given by

$$s_{1,2} = \mp \mathrm{i}\Omega - 2\nu k^2. \tag{18}$$

Equation (18) expresses the well-known dispersion relation for gravity–capillary waves on the free surface of a deep weakly viscous liquid. By using the residue theorem, one can find

$$h(r, t) = \frac{1}{\rho_0} \int_0^\infty k^2 \hat{\Pi}(k) \frac{\sin(\Omega t)}{\Omega} \mathrm{e}^{-2\nu k^2 t} J_0(kr)\, \mathrm{d}k. \tag{19}$$

From (18), (19), the condition $\nu k^2/s \ll 1$ ensures the small damping of disturbances over the period of oscillations.

To illustrate the shape of surface disturbances according to (19) a particular $\Pi(r)$ distribution must be chosen. In experiments described below a discharge CO_2-laser has been used, with the TEM_{00}-mode of radiation being selected. Therefore, the laser energy cross-sectional distribution was well defined by a Gaussian law:

$$w(r) = (\mathscr{E}_0/\pi b^2) \exp(-(r/b)^2)$$

($\mathscr{E}_0$ is the total energy of the laser pulse). Taking into account the experimentally obtained threshold for the development of intense evaporation from a liquid surface heated by laser radiation (Alekseev *et al.* 1987), a parabolic law was chosen to approximate the recoil pressure momentum surface distribution:

$$\Pi(r) = \Pi_0(1 - (r/a)^2).$$

Given the value of laser energy density threshold w_{thr}, the effective radius a is expressed via the measured radius b as

$$a = \left[\ln\left(\frac{\mathscr{E}_0}{\pi b^2 w_{\mathrm{thr}}}\right)\right]^{\frac{1}{2}} b. \tag{20}$$

The Fourier–Bessel transform for a parabolic law gives

$$\hat{\Pi}(k) = (2\Pi_0/k^2)\, J_2(ka). \tag{21}$$

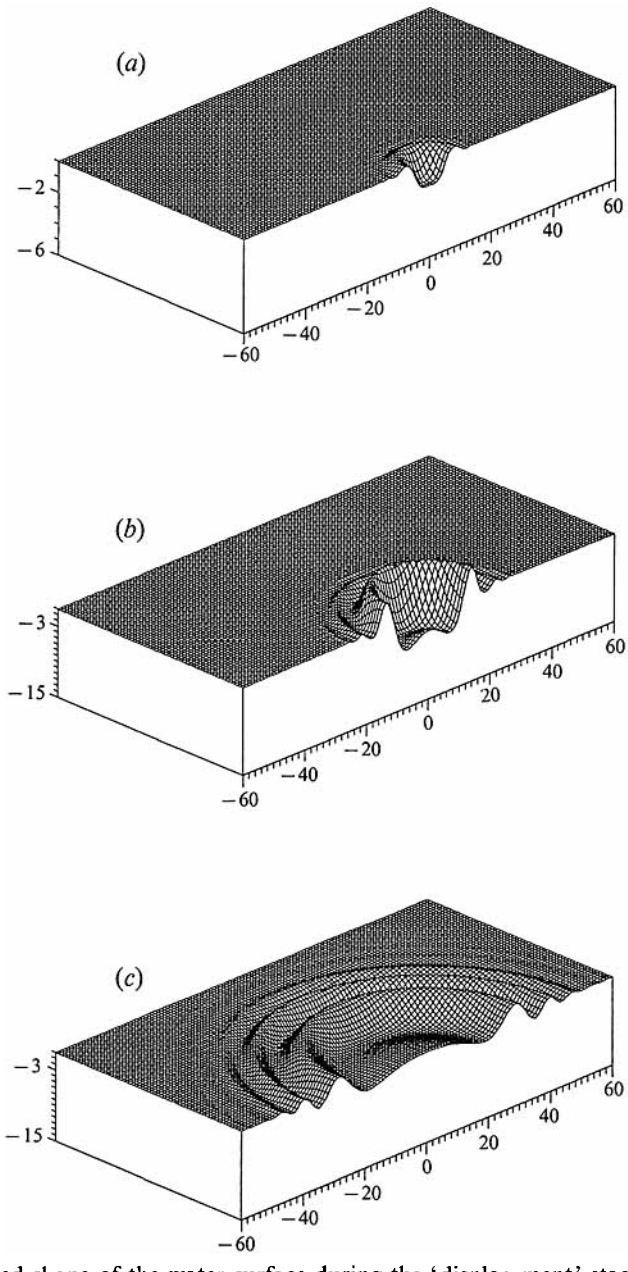

FIGURE 2. Calculated shape of the water surface during the 'displacement' stage: (*a*) $t = 6$ ms; (*b*) $t = 15$ ms; (*c*) $t = 40$ ms. The vertical scale corresponds to normalized displacements h/Π_0 [mm/Pa s] ($\Pi_0 = 1$ Ps s for (*a*) and $\Pi_0 = 0.1$ Pa s for (*b*, *c*). Tick mark distance for the horizontal scale is 0.23 mm. Impact spot radius $a = 2.0$ mm.

The three-dimensional plots of figure 2 illustrate the liquid surface shapes calculated in accordance with (19) and (21). The plots help to show the dynamics of surface motion in the impact region and the very beginning of the GCW-generation process, which will be considered in detail in §4. A comparison of calculations with experiments is made in §3.3.

The process of boundary deformation of highly viscous fluids, i.e. in glycerol with

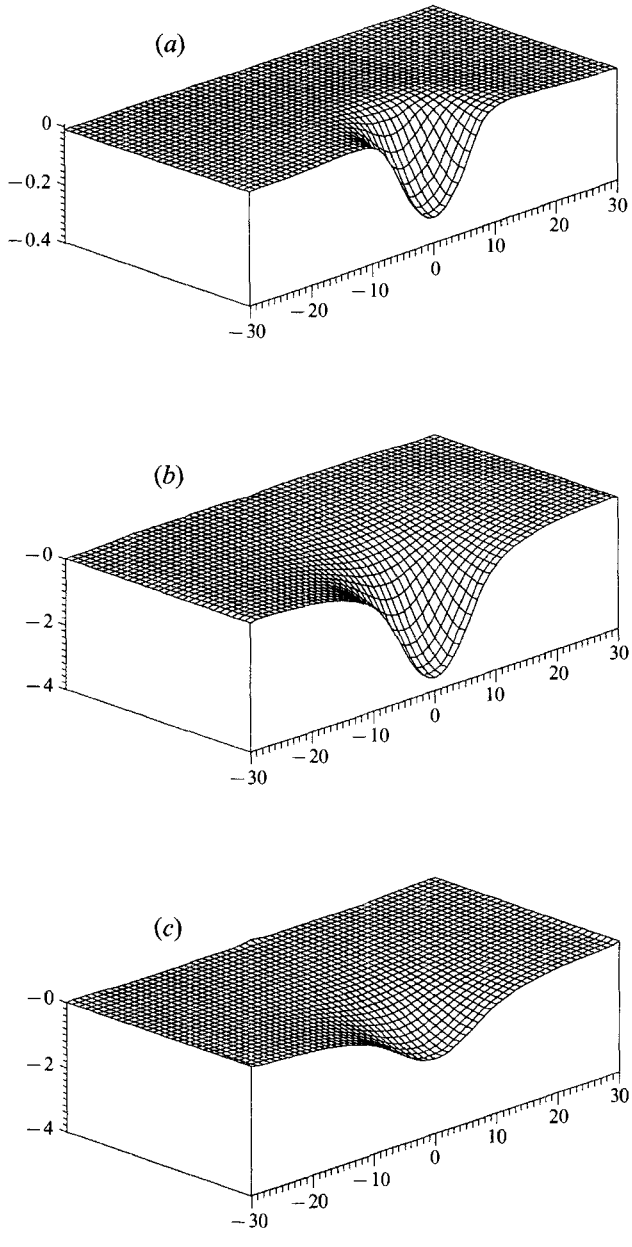

FIGURE 3. Calculated shape of the 'cold' (20 °C) glycerol surface during the 'displacement' stage: (*a*) $t = 0.8$ ms; (*b*) $t = 8$ ms; (*c*) $t = 40$ ms. Vertical scale as figure 3. Tick mark distance for horizontal scale is 0.27 mm, $a = 2.00$ mm.

viscosity $\nu = 1.2 \times 10^{-3}$ m^2/s (at 20 °C) three orders of magnitude greater than for water, shows a different development. Flor glycerol the following condition holds:

$$\nu k^2/s \gg 1.$$

In this limit the poles of the integrand in (17) are given by

$$s_1 = -\Omega^2/2\nu k^2, \quad s_2 = -2\nu k^2.$$

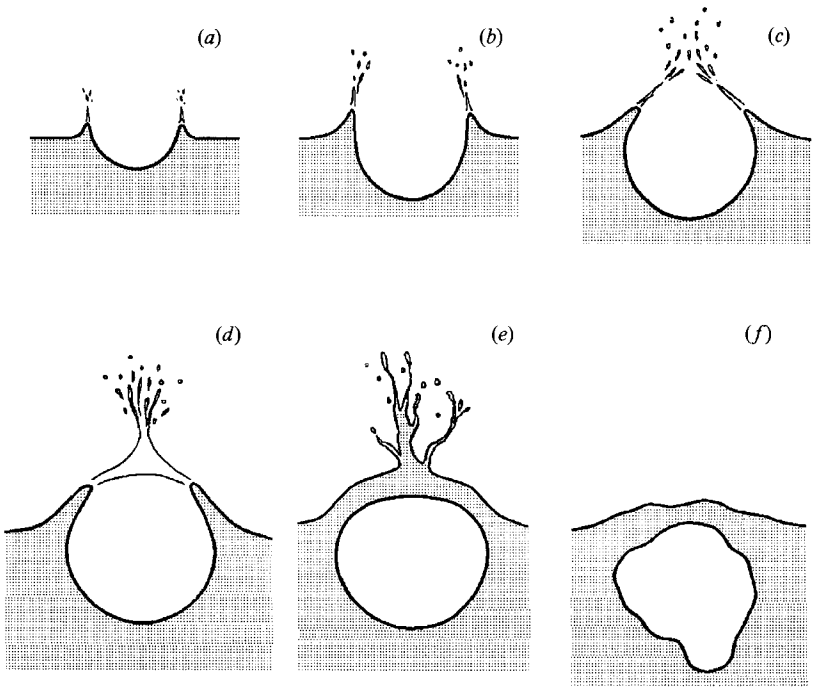

FIGURE 4. Sketch of surface disturbance evolution in the case of high-amplitude recoil pressure momenta.

Both roots are real and negative, so the surface motion will be aperiodical and rapidly decreasing. The correspondent integral expression for $h(t, r)$ is of the form

$$h(r,t) = \frac{1}{\rho_0}\int_0^\infty k^2 \hat{\Pi}(k) \frac{\mathrm{e}^{-(\Omega^2/2\nu k^2)t} - \mathrm{e}^{-2\nu k^2 t}}{2\nu k^2 - \Omega^2/2\nu k^2} J_0(kr)\,\mathrm{d}k. \tag{22}$$

The evolution of surface disturbances described by (22) is shown in figure 3 for glycerol (at 20 °C). In this case spreading GCWs are not produced.

3.2. *Description of cavity expansion*

Equations (19) and (22) are valid in the linear approximation: $h \ll a$. When $h > a$ the problem is essentially nonlinear and can hardly be treated analytically, though a set of features revealed during experimental investigation of the surface deformation process enabled us to develop theoretical model for this case. In a wide range of laser energies the deformed region of the surface turned out to take the shape of a hemisphere which expands into the fluid over a definite time period. A qualitative sketch of surface disturbance evolution is presented in figure 4 (the sketch is based on experimental data displayed on the shadowgraphs of §3.3). For the time moments corresponding to figure 4*b–d*), the flow is generally determined by the law of hemisphere expansion $R(t)$, with radius R being measured from the centre of the initial impact spot on the surface.

Let E_0 and R_0 denote the motion energy and the hemisphere radius at a starting time t_0; then the energy balance equation is written as

$$\pi\rho_0 R^3(t)\,(\partial R/\partial t)^2 + \Delta F = E_0, \tag{23}$$

where the free energy increment ΔF consists of the surface deformation energy which can be evaluated as $\pi\sigma(R^2(t) - R_0)$, and the potential energy variation in the gravity

field. Following the reasoning of Landau & Lifshitz (1986, §61), we consider ΔF to be determined primarily by the surface deformation energy when the radius in question is sufficiently small: $(2\sigma/g\rho_0) > R$. Then, provided the initial energy of expansion E_0 is large enough, so that for a time period $[t_0, t_k]$ the condition $E_0 \gg \pi\sigma R^2(t)$ is valid, (23) is easily integrable:

$$R = \{R_0^{\frac{5}{2}} + \tfrac{5}{2}(E_0/\pi\rho_0)^{\frac{1}{2}}(t-t_0)\}^{\frac{2}{5}}, \quad t_0 \leqslant t \leqslant t_k. \tag{24}$$

From the drawings of figure 4 it follows that the initial radius R_0 may be taken approximately equal to the characteristic radius of the impact spot: $R_0 \approx a$. For a parabolic distribution of recoil pressure momentum $\Pi(r)$ the total flow energy T_{in} defined by (4) is given by

$$T_{\text{in}} = \tfrac{16}{15}\Pi_0^2 a/\rho_0 \approx a\Pi_0^2/\rho_0, \tag{25}$$

in full agreement with estimation (5). It is obvious that when

$$\Pi_0 \gg (a\sigma\rho_0)^{\frac{1}{2}} \tag{26}$$

one can neglect the share of total energy expended on the deformation of the initially flat liquid surface into the hemisphere of radius a, and consider $E_0 \approx T_{\text{in}}$ in (23) and (24). Note that unless condition (26) is satisfied, all the kinetic energy is already transferred into surface deformation energy for $R \leqslant a$ and the regime considered does not appear. Thus, under the assumption stated, the law of hemisphere expansion can be written as

$$R(t) = \{\tfrac{5}{2}\rho_0(a/\pi)^{\frac{1}{2}}\Pi_0(t-t_0) + a^{\frac{5}{2}}\}^{\frac{2}{5}}. \tag{27}$$

In deriving (27) we have not taken into account viscous damping. Let us determine the consistency of the assumption. The rate of kinetic energy decrease due to viscosity is given by (6). By substituting (27) one can find:

$$\frac{\partial T}{\partial t} = -\frac{6\nu}{\rho_0}\frac{\Pi_0^2 a}{R^2(t)}.$$

For the hemisphere expansion from initial radius a to a radius R the total amount of dissipated energy is

$$\Delta T = 12\pi^{\frac{1}{2}}\Pi_0 a\nu\{(R/a)^{\frac{1}{2}} - 1\}.$$

Hence, the influence of viscosity is negligible when

$$\Delta T/E_0 \approx 12\pi^{\frac{1}{2}}(\nu\rho_0/\Pi_0)(R/a)^{\frac{1}{2}} \ll 1.$$

This condition held for all experimentally investigated liquids except for glycerol.

Thus, the theoretical examination gives the following flow features. Under conditions (7) the surface displacement develops the shape described by (19) and (22). The initial disturbance results in the formation of a GCW-packet spreading axially symmetrically out of the impact region. Provided the average surface density of recoil momentum satisfies condition (26), the motion is of essentially nonlinear character: after the short transient stage the surface takes the shape of a hemisphere expanding into the bulk of the fluid in accordance with the law (27). Note that the theoretical conclusions about the existence of an $R \sim \Delta t^{\frac{2}{5}}$ dependence are consistent with the data reported by Minin (1964). He examined experimentally cylindrical and point explosions on a free liquid surface and reported that the motion of liquid induced by the point surface explosion is a nearly self-similar expansion with the time-dependence power $n \approx 0.38$. Note also, that the time dependence $R \sim t^{\frac{2}{5}}$ for the radius of abrupt change of density follows from a theoretical analysis of a 'very intense explosion' (Sedov 1946). Actually, by neglecting the surface tension and taking $R_0 \ll R$ we could reduce our problem to the examination of the isobaric expansion of the spherical cavity in a boundless fluid which is determined by only two parameters, ρ_0 and E_0, in full agreement with conclusions of 'very intense explosion' theory.

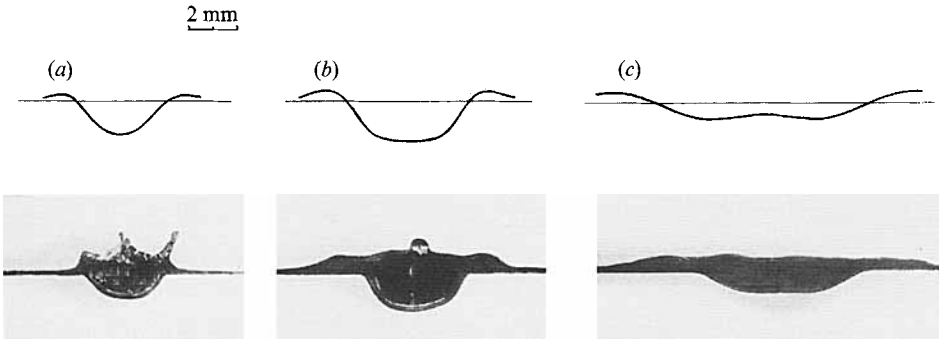

FIGURE 5. Comparison of calculated and experimentally obtained profiles of a water surface after a laser blast. Impact spot radius $a = 2.1$ mm. Recoil pressure momentum $\Pi_0 = 1$ Pa s. (*a*) $t = 1.5$ ms; (*b*) $t = 6.0$ ms; (*c*) $t = 15.0$ ms.

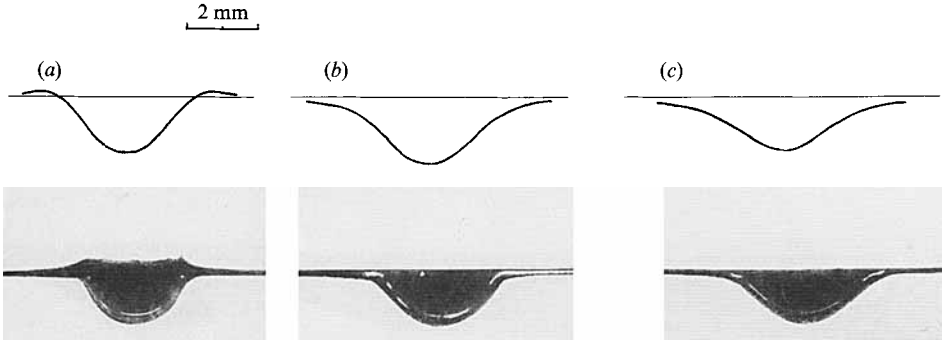

FIGURE 6. Comparison of calculated and experimentally obtained profiles of a glycerol surface at 24 °C after a laser blast. Impact spot radius $a = 1.8$ mm. Recoil pressure momentum $\Pi_0 = 6.7$ Pa s. (*a*) $t = 0.8$ ms; (*b*) $t = 8.0$ ms; (*c*) $t = 20.0$ ms.

Liquids	ρ_0 (kg/m^3)	σ (N/m)	ν (m^2/s)	α (cm^{-1})	L (kJ/kg)	w_{thr} (J/cm^2)	w^* (J/cm^2)
Water	998	0.073	1.00×10^{-6}	1080	2256	1.4	2.1
Ethanol	789	0.022	1.52×10^{-6}	480	840	2.1	2.7
Glycerol	1260	0.065	$4. \times 10^{-5}$ (70 °C) 7.9×10^{-4} (24 °C)	3640	962	1.6 (70 °C) 3.9 (24 °C)	2.2 (70 °C) –

TABLE 1. Physical parameters of liquids under investigation. The data are taken from *Tables of Physical Quantities: Handbook* (ed. I. K. Kikoin) – Moscow: Atomizdat, 1976; *The Sadtler Handbook of Infrared Spectra*. Philadelphia: Sadtler Res. Labs, 1978.

In the intermediate case of displacements $h \sim a$ the motion could also be qualitatively described by the expressions from the linear approximation as it will be shown below, with nonlinearity being appreciable only for a long-time GCW train propagation process.

3.3. *Experimental investigation of surface disturbances*

To verify the validity of the theoretical analysis and to measure directly the value of recoil pressure momentum transferred to the surface an experiment with optical registration of laser-induced surface disturbances was done.

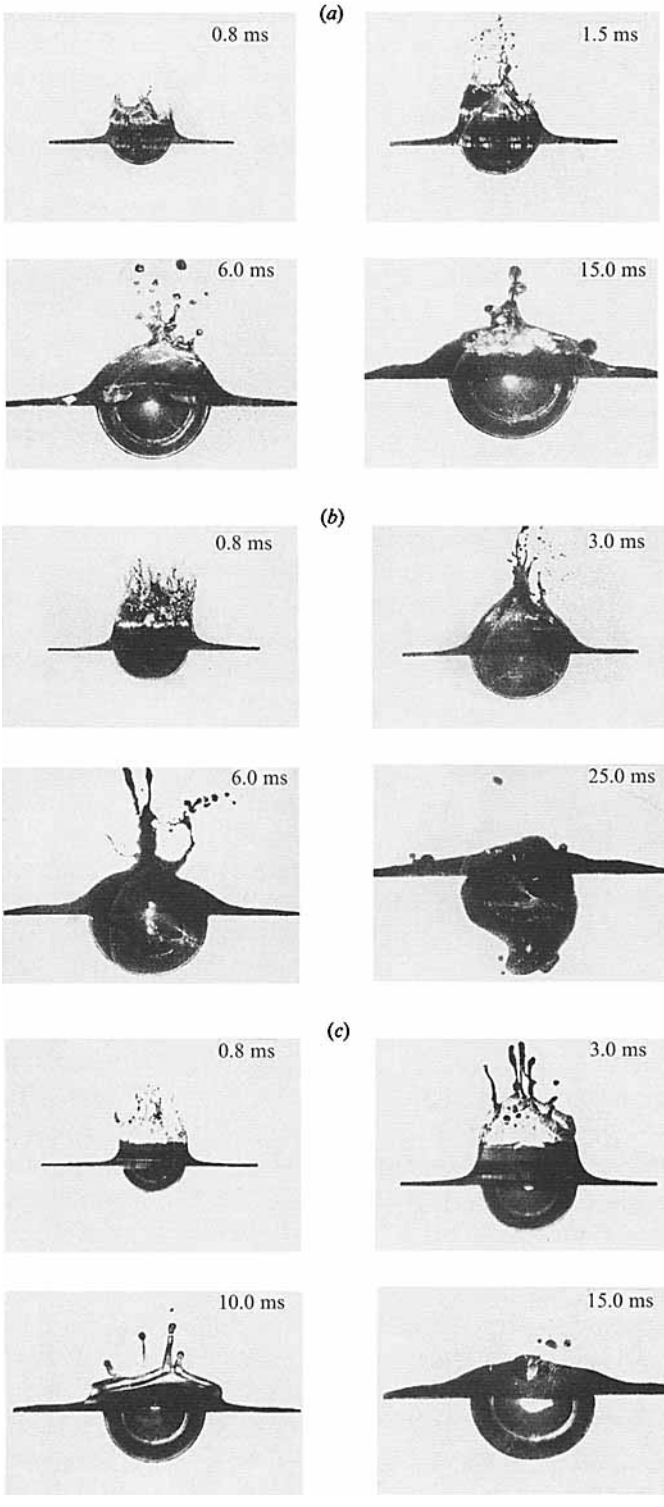
(a)
0.8 ms
1.5 ms
6.0 ms
15.0 ms
(b)
0.8 ms
3.0 ms
6.0 ms
25.0 ms
(c)
0.8 ms
3.0 ms
10.0 ms
15.0 ms

A pulsed electric-discharge TEA CO_2-laser was used as the source of radiation. The corresponding absorption coefficients α for the liquids under study are presented in table 1. The total energy of the CO_2-laser pulse was varied in the range 0.05–0.6 J and controlled by a pass-wire differential bolometer. The laser radiation was focused onto the surface of the liquid contained in a quartz cuvette by means of a KCl-lens and a copper mirror. The cuvette was equipped with a heating system to adjust the temperature of the fluids over a wide range. The surface disturbances were visualized by the shadowgraph technique, with a Nd^{3+}:YAG-laser being used as a flashlight (the pulse width was equal to 30 ns and the wavelength after frequency doubling was 0.53 μm). The gate of a photocamera was synchronized with the CO_2-laser shock. The Nd^{3+}:YAG-laser pulse was driven behind the shock with a controlled time delay (the accuracy was better than 1 μs). The detection was carried out in the time-delay range 0.2–100 ms which enabled us to investigate accurately the shape of surface disturbances along with the dependence of surface displacement amplitude on the laser pulse energy and time. The photo-detection of a standard object located in the impact region revealed that the accuracy of vertical displacement measurements was ≈ 0.1 mm. To minimize the effect of the meniscus on the fluid–wall interface the cuvette was filled precisely up to the brim and there was virtually no meniscus formed at all.

In the course of the experiments appreciable surface disturbances were found to arise only when the laser energy was above a threshold value w_{thr} specific to the liquid. The reason of this is the lack of intense evaporation for small laser energies. The values of w_{thr} are given in Table 1 in comparison with the specific heats of vaporization L. Note that the detection of acoustic transients generated by recoil pressure impact also revealed threshold laser densities and the exceeding of them resulted in a sharp increase of the acoustic pulse amplitude. The threshold value $w_{thr} = 1.4$ J/cm^2 we found for water is virtually coincident with the value 1.5 J/cm^2 obtained in the acoustic experiments of Vitshas & Korneev (1987).

The amplitude of the surface displacement had nearly reached the order of the radius a magnitude when the threshold value was exceeded by 30–40%. These displacements could not be described in the framework of the linear approximation. Meanwhile, a satisfactory agreement between calculated and experimentally measured surface shapes was found even for $h \sim a$, when shadowgraphs are more distinct. In figure 5 the water surface profiles for three instants of time are compared with the results of calculations for laser energy density $w = 2.0$ J/cm^2. (The droplet-like disturbance emerging in figure 5 at 6.0 ms is not a feature of a Rayleigh-type jet but rather a consequence of irregular motion of liquid on the ridge of the deforming surface, cf. the photo for 1.5 ms.) In figure 6 an analogous comparison is made for glycerol with a temperature of 24 °C ($w = 4.3$ J/cm^2). The measurements were also carried out in ethanol and glycerol heated up to 70 °C. Qualitatively, the dynamics of surface displacement are similar to those represented in figure 5. When $h \sim a$, the expressions of the linear approximation describe the experimental data well only on a small timescale. The nonlinearity appearing at later times leads to an appreciable discrepancy between predicted GCW-profiles and measured ones for this case (for details see §5).

As mentioned above, for greater energies the deformed surface at a particular stage takes the shape of hemisphere expanding into the bulk of the liquid. The evolution of the disturbance is displayed on the photos in figure 7 (*a–c*) for the three fluids investigated. From the data of a set of experiments the variation of surface

FIGURE 7. Dynamics of a laser-blast-driven hemisphere expansion and bubble formation for (*a*) water, (*b*) ethanol and (*c*) 'hot' (70 °C) glycerol. The values of laser energy density are: for water $w \approx 4.7$ J/cm^2; for ethanol $w \approx 5.8$ J/cm^2; for glycerol $w \approx 7.6$ J/cm^2.

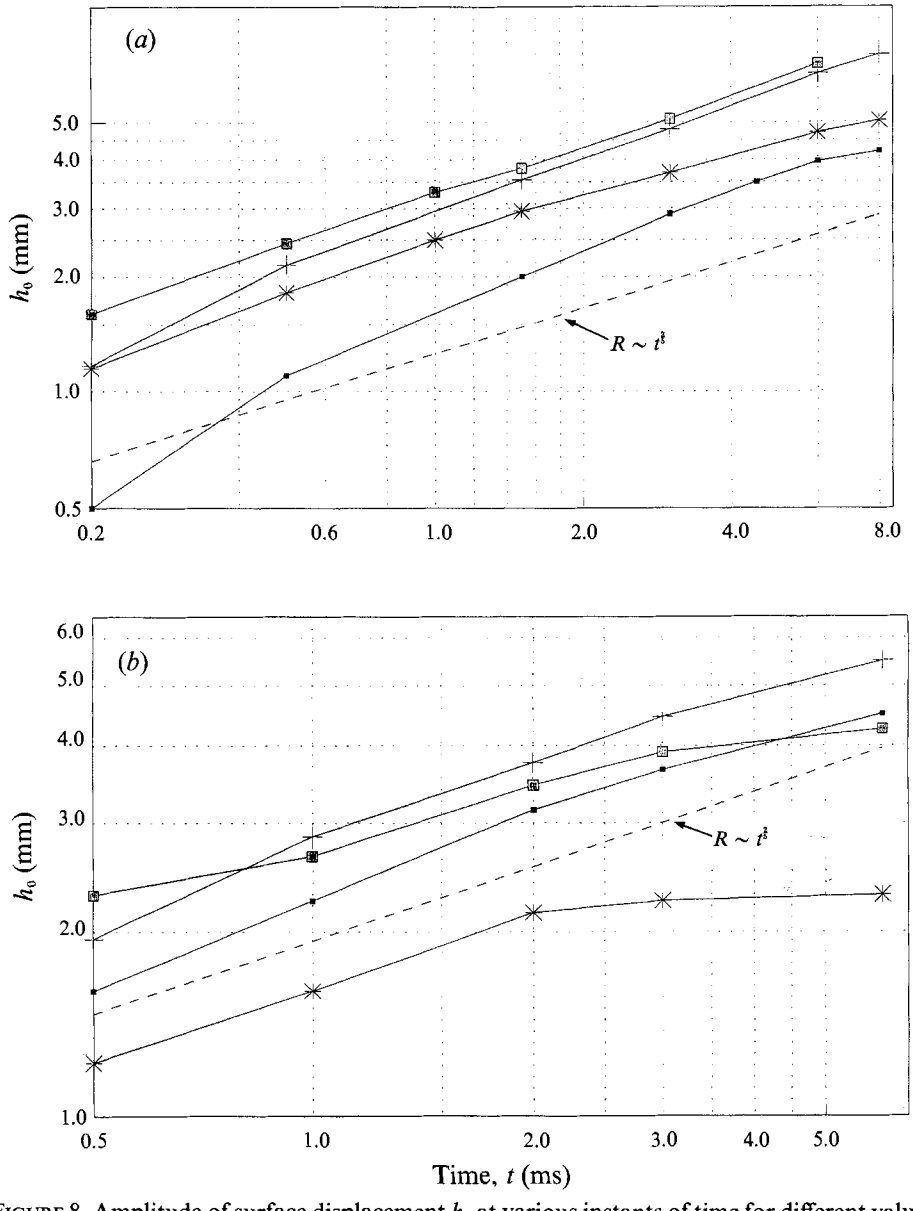

FIGURE 8. Amplitude of surface displacement h_0 at various instants of time for different values of laser energy density: (*a*) in water $w \approx 2.8$ J/cm^2 (■), 5.7 J/cm^2 (+); ethanol 4.25 J/cm^2 (*), 5.7 J/cm^2 (▨); (*b*) in glycerol (70 °C) $w \approx 4.2$ J/cm^2 (■), 6.5 J/cm^2 (+); glycerol (24 °C) $w \approx 6.6$ J/cm^2 (*), 11.1 J/cm^2 (▨).

displacement amplitude h_0 with time t was plotted for various laser energies (see figure 8*a*, *b*). Here the time dependence $h_0(t)$ for 'cold', 24 °C, glycerol is also presented for comparison, though the surface shape is analogous to that displayed in figure 6. From figures 7 and 8 it follows that for all laser energies $\mathscr{E}$ above a certain minimal value there exists a time interval for which the surface shape is hemisphere-like and its expansion law is $R(t) \sim t^{\frac{2}{5}}$, in accordance with (22). Therefore, by determining experimentally the $R(\mathscr{E})$ dependence for time instants within the interval of validity of the $R(t) \sim t^{\frac{2}{5}}$ law, one can find the relationship between Π_0 and $\mathscr{E}$. In figure 9 the

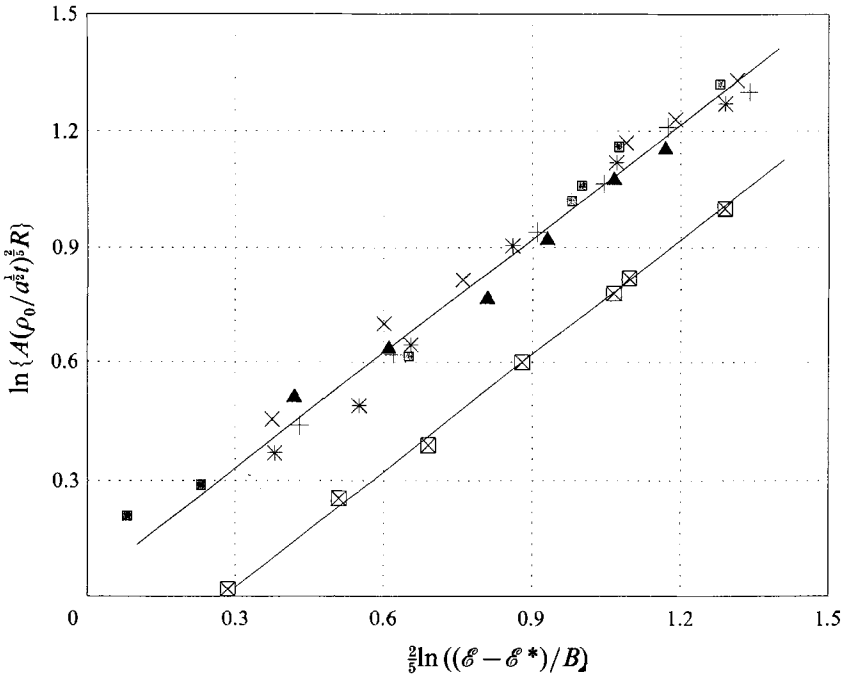

FIGURE 9. Dependence of hemisphere radius R on laser energy $\mathscr{E}$ for instants of time in the interval of validity of the $R \sim t^{\frac{2}{5}}$ law. Experimental points correspondent to the spot radius $a = 1.8$ mm: water, $t = 1.5$ ms (▲), 3 ms (+); ethanol, $t = 1.5$ ms (*), 3 ms (▨); glycerol, (70 °C) $t = 3$ ms (×). Experimental points correspondent to the spot radius $a = 2.75$ mm: water, $t = 3$ ms (⊠).

dependence $R(\mathscr{E})$ is plotted for two values of impact spot radius a in logarithmic coordinates chosen in regard to (22). The value $\mathscr{E}^*$ has to be determined in the experiment and corresponds to the energy needed to displace the liquid surface from equilibrium to the depth $h_0 = a$. The constants A and B make the logarithm arguments dimensionless and, for data presentation convenience, are taken equal to $A = 1.1\ (\mathrm{sm/kg})^{\frac{2}{5}}$, $B = 1.7 \times 10^{-2}$ J. Figure 9 shows, given fixed impact spot radius a, that experimental data lie along the same line for all fluids under study. An approximation of the line gives the following relationship between R and $\mathscr{E}$:

$$R = \kappa(t(\mathscr{E}-\mathscr{E}^*))^{\frac{2}{5}}, \tag{28}$$

where κ is the common coefficient of proportionality depending upon the laser beam radius. Comparing (28) with the theoretical expression (24) and neglecting the difference between the laser beam radius b and the pressure impact spot radius a (see (20)), we can write:

$$\Pi_0 \approx \gamma(w-w^*). \tag{29}$$

The values of the $w^* = \mathscr{E}^*/\pi a^2$ are given in table 1. Note that (29) is valid only when $(w-w^*) \gg \max((a\sigma\rho_0)^{\frac{1}{2}}/\gamma, \nu\rho_0/\gamma)$ in accordance with (7). The coefficient γ turned out to be the same for water, ethanol and 'hot' (70 °C) glycerol: $\gamma \approx 2.4 \times 10^{-4}$ s/m. It does not depend on the radius a in the range examined: $a = 1$–3 mm. According to (29) the experimentally obtained values of total recoil pressure momentum for water lie in the range: $\Pi_0 = (2.4$–$15.1)$ Pa s for $w = (3.1$–$8.4)$ J/cm^2. It should be pointed out for comparison that in an analogous experimental situation (the CO_2-laser irradiation of water) for greater beam radius (≈ 5 mm) Vitshas, Korneev & Menakhin (1987)

reconstructed from indirect acoustic measurements the value of recoil momentum $\Pi_0 \approx 1$ Pa s for $w \approx 0.85$ J/cm^2. The increase of the Π_0/w relation seems to be explained by the higher efficiency of recoil force action under the conditions of a prolongated plane configuration of vapour ejection.

The $\Pi_0(w)$ dependence found permits us to estimate the share of laser energy transferred into the energy of liquid motion. The latter is expressed via Π_0 according to (25). Taking into account (29) one obtains:

$$T_{\text{in}} \approx \frac{a}{\rho_0}\gamma^2(w-w^*)^2,$$

For water, taking $a = 2\times10^{-3}$ m and $\mathscr{E} = 0.5$ J, one obtains $T_{\text{in}} \sim 3.5$ mJ. Thus, the coefficient of transformation of laser energy to hydrodynamic energy is approximately equal to $\approx 1\,\%$. It increases with the increase of laser energy.

The features of liquid surface disturbances induced by laser heating established here are important for developing of an adequate theory of interaction of laser light with dielectric liquids.

4. Laser-induced GCW-trains

4.1. *Theoretical description*

In the previous section the initial stage of the development of laser-induced surface disturbances was considered. In inviscid liquid (water, ethanol etc.) the initial surface displacement leads to the generation of GCW-trains spreading out radially from the impact zone.

Here simple analytical expressions to describe these GCWs will be obtained and a technique to probe the physical–chemical properties of contaminated film-covered interfaces will be proposed.

4.1.1. *GCWs on film-covered interfaces*

The process of GCW-propagation on film-covered surfaces (these comprise most real interfaces not cleaned specially) is related to the reversible transient variations of physical–chemical parameters of the surface. Therefore, (15*b*), which claims the equality of tangential stress components on the surface, in the case of film-covered surfaces has a non-zero term on the right-hand side. Indeed, the deformation of a clean surface does not lead to local variations of surface tension. Given a film-covered surface, compression/expansion of the film results in substantial fluctuations of the tension of the liquid–film system. To characterize quantitatively the phenomenon, the surface dilational modulus was introduced (Lucassen-Reynders & Lucassen 1970):

$$\epsilon = A_{\text{s}}\,\mathrm{d}\sigma/\mathrm{d}A_{\text{s}},$$

where A_{s} is the area of a surface element. So, (15*b*) has to be rewritten in the form

$$\eta\left(\frac{\partial^2}{\partial z^2}+k^2\right)\hat{\psi} = -\frac{\epsilon}{s}k^2\frac{\partial}{\partial z}\hat{\psi},$$

and instead of the system of equations (16) one must solve the following system of linear equations:

$$(2\nu k^2-(\epsilon/s\rho_0)k^3)\,A+((k^2+m^2)\,\nu-(\epsilon/s\rho_0)k^2m)\,B=0, \tag{30a}$$

$$(2\nu k^2+s+\Omega^2/s)\,A+(2\nu km+\Omega^2/s)\,B=\hat{\Pi}(k)/\rho_0. \tag{30b}$$

The general scheme of solution presented in §2.1 holds except for the final dispersion relation. Let the roots of the $\det(s) = 0$ equation for system (30) be sought in the form:

$$s = i\omega_0 + \beta, \tag{31}$$

where β denotes the attenuation coefficient of a GCW on the liquid surface. We shall be interested in the solution which satisfies the condition $\beta/\omega_0 \ll 1$. In fact, as in §2.1, this condition restricts the value of liquid viscosity. The numerical calculations of Lucassen-Reynders & Lucassen (1970) have shown that among the roots of the $\det(s) = 0$ equation there exist those that do not satisfy the condition $\beta/\omega_0 \ll 1$ even in inviscid liquids. But they do not correspond to spreading GCWs and in the linear approximation do not distort the GCW-profiles much, at a sufficiently long distance from the origin. Provided the roots are in the form of (31), the equation $\det(s) = 0$ splits to given expressions for the real and the imaginary parts of s. Accurate calculations, nevertheless, reveal that the imaginary part (ω_0) differs from Ω by no more than 3% over the capillary frequency spectrum. Thus, with the given accuracy in the equation for β one can substitute Ω for ω_0 making use of Kelvin's dispersion law. Then, the expression for β is given by (Levich 1962):

$$\beta = -2\nu k^2 \frac{[\Omega/(32\nu k^2)]^{\frac{1}{3}} q^2\tilde{\epsilon}^2 - q\tilde{\epsilon}/\sqrt{2} + 1}{q^2\tilde{\epsilon}^2 - \sqrt{2}\, q\tilde{\epsilon} + 1}, \tag{32}$$

where $\tilde{\epsilon} = \epsilon/\rho_0$, $q = k^2/\Omega^2(\Omega/\nu)^{\frac{1}{2}}$. To obtain (32) the surface elasticity modulus was assumed to be a real quantity. This implies that the compression/expansion deformation is instantaneously followed by the variation of surface tension. This is the case of a pure elastic interface. There are numerous dynamic surface phenomena, however, which result in a time delay between deformation $\mathrm{d}\ln(A_s)$ and surface tension variation $\mathrm{d}\sigma$. Characteristic examples are the process of diffusional exchange between a contamination film adsorbed on the surface and the contamination substance dissolved in the bulk of the liquid; the relaxation through micellar breakdown; the process of reorientation of surfactant macromolecules on the surface, etc. (see the review of Van den Tempel & Lucassen-Reynders 1983). The interfaces with pronounced relaxation process are said to be viscoelastic ones, with their ϵ modulus being complex. In any case the presence of a film leads to substantial increase of the attenuation coefficient, i.e. to more rapid GCW damping. Also, the frequency dependence of attenuation is varied. Van den Tempel & Lucassen-Reynders (1983) have shown that the existence of time constants which are specific for particular relaxation processes gives an opportunity to identify the process by examining its $\beta(k)$ dependence. To measure the $\beta(k)$ dependence one can detect the spatial (or temporal) attenuation of GCW-trains propagating on the surface. These considerations were on the basis of a dynamic diagnostic technique proposed here to probe the interface by means of laser-induced GCW-trains.

4.1.2 *Asymptotic expressions for GCW-packets*

Expression (19) makes it possible to describe any stage of surface disturbance evolution. But at large distances from the impact region it is worth using the asymptotic expressions for the relationship between the GCW-train profile (or its spectrum) and the attenuation coefficient β, which is convenient for diagnostics.

In remote detection of low-amplitude ripples the measured parameter was the inclination angle $\phi(r, t) = \arctan(\partial h/\partial r)$ instead of the displacement $h(r, t)$ itself. Therefore asymptotic expressions for GCW inclination angles are derived below. In the

linear approximation the angles are quite small (experimental data presented in §4.2 reveal the appearance of nonlinearity for $\phi \geqslant 0.1$ rad), so with an accuracy $\approx 0.1\,\%$ we can take $\phi(r,t) \approx \partial h(r,t)/\partial t$. Expression (19) for inclination angles can be written as

$$\phi(r,t) = -\int_0^\infty k^3 \hat{\Pi}(k) \frac{\sin(\Omega t)}{\Omega} e^{-\beta t} J_1(kr)\,dk. \tag{33}$$

The technique to obtain the asymptotic estimation of integral (33) is well-known (see, for example Lamb 1932). In the case under consideration one should make use of Bessel function asymptotics:

$$J_n(x)|_{x\to\infty} \sim (2/\pi x)^{\frac{1}{2}} \cos(x - \tfrac{1}{2}n\pi - \tfrac{1}{4}\pi).$$

Then, the application of the stationary phase method of the integral (33) gives the following expression for the inclination angles:

$$\phi(r,t) \approx \sum_{i=1,2} \frac{2}{\rho_0} \frac{\hat{\Pi}(k_i) k_i^{\frac{5}{2}}}{(r,t)^{\frac{1}{2}} \Omega(k_i)} \frac{\exp\{-\beta(k_i)\,t\}}{|\partial^2 \Omega/\partial k^2|_{k=k_i}|^{\frac{1}{2}}} \sin(\theta(k_i)), \tag{34}$$

where the phase $\theta(k_i) = \Omega(k_i)\,t - k_i r$. The summation in (34) is performed for two points of stationary phase that correspond to the roots of the equation

$$\mathscr{U} = d\Omega/dk = r/t, \tag{35}$$

where $\mathscr{U}$ is the group velocity of the wave packet. Equation (35) has two different roots related to the gravitational and capillary parts of the surface wave spectrum when

$$r/t > \mathscr{U}_{\min} = \{3((2-\sqrt{3})/\sqrt{3})^{\frac{1}{2}}\}^{\frac{1}{2}} (\tilde{\sigma} g)^{\frac{1}{4}} \tag{36}$$

(for example, for water $\mathscr{U}_{\min} \approx 17.7$ cm/s). In the case of $r/t \leqslant \mathscr{U}_{\min}$ a more accurate analysis is needed, with the next terms of phase development in (33) being included. Taking into consideration only the range of spectral components of the wave packet of appreciable amplitude, we shall further restrict ourselves to the case of the inequality (36) being valid. For a given point of observation r the condition (36) puts an upper limit on the time interval wherein (34) may be used. The lower limit is determined by the general condition of validity of the stationary phase method (Lamb 1932):

$$\frac{\partial f(k)}{\partial k^3} \left| \frac{\partial^2 f(k)}{\partial k^2} \right|^{-\frac{3}{2}} \ll 1, \tag{37}$$

where $f(k) = \Omega(k)\,t - kr + \frac{3}{4}\pi$ is the phase function. Numerical computer calculations were conducted to compare directly the GCW-profiles given by the integral relation (33) and the asymptotic expression (34). The results of both calculations were found to coincide (with an accuracy better than 1%) in the time interval determined by conditions (36), (37).

In addition to the inclination angle profile it is worth obtaining the explicit expression for the spectrum $\hat{\phi}(\omega, r)$. Equation (34) can be rewritten as

$$\phi(r,t) = \sum_{i=1,2} g(t) \sin(\Omega(k_i)\,t - k_i r),$$

where $g(t)$ is a slowly varying (compared to the oscillating multiplier) function of t. Then the integral expression for the spectrum

$$\hat{\phi}(\omega, r) = \sum_{i=1,2} \int_{-\infty}^{+\infty} g(t) \sin(\Omega(k_i)\,t - k_i r)\, e^{-i\omega t}\,dt \tag{38}$$

can also be evaluated by means of the stationary phase method. Taking into account the exponential form of the sine function, (38) consists of four integrals. Two of them are negligibly small as their phases have no stationary points. For the other two the condition of stationarity claims $\Omega(k_{1,2}) = \omega$. So, the two terms corresponding to the gravitational and the capillary part of the spectrum in the time-domain approach, (34), are combined to give the unified gravitation–capillary spectrum of surface wave packets:

$$|\hat{\phi}(\omega, r)| \approx \frac{2}{\rho}\left(\frac{2\pi}{r}\right)^{\frac{1}{2}} k^{\frac{5}{2}}(\omega) \frac{\hat{\Pi}(w)}{w\mathscr{U}(\omega)} \exp\left\{-\frac{\beta(\omega)}{\mathscr{U}(\omega)} r\right\}. \tag{39}$$

The validity of this expression was also proved by comparison with computer calculations on the integral (33). The complete identity of both spectra in the whole range of spectral components of appreciable amplitude was established.

The formula (39) gives a simple relationship between the GCW-spectrum $\hat{\phi}(\omega, r)$ and the frequency dependence of the attenuation coefficient $\beta(\omega)$ which is of importance for characterization of surface properties. Thus, experimental registration of $\beta(\omega)$ enables one to probe the cleanliness of an air–liquid interface and to investigate the relaxation processes accompanying the propagation of GCW-trains on a film-covered surface. The results of calculations of laser-induced GCW-trains on clean and contaminated water surfaces are presented in figure 10. The temporal profile of the ripples is displayed with respect to the phase $\theta(k_0)$, with the reference spectral component k_0 being chosen to correspond to the wavelength that equals the impact spot diameter: $k_0 = \pi/a$. Displayed here are the GCW-profiles calculated from formulae (32) and (34) for two types of interfaces: a GCW-train on a clean surface is represented by a solid line (surface dilational modulus $\epsilon = 0$) and that on an elastic film-covered interface ($\epsilon = 10^{-2}$ N/m) by a dashed line. It is obvious that the presence of the film results in the attenuation of high-frequency components of the GCW-spectrum. The combined action of dispersion and attenuation leads to the rapid monochromatization of the packet as it propagates to larger distances.

4.1.3. *Diagnostic features of laser-induced GCWs*

The theoretical description given of laser-induced GCW-packets suggests the use of the remote sensing technique to investigate the properties of air–liquid interfaces by examining the attenuation spectrum $\beta(\omega)$. Measurements are taken from the observation points, r_1 and r_2, to determine relation of the amplitude spectra of GCW-trains. Then, in accordance with (39), the attenuation spectrum is given by

$$\beta(\omega) = -\frac{U(\omega)}{r_2 - r_1} \ln\left\{\left(\frac{r_2}{r_1}\right)^{\frac{1}{2}} \frac{|\hat{\phi}_{\exp}(\omega, r_1)|}{|\hat{\phi}_{\exp}(\omega, r_2)|}\right\}, \tag{40}$$

where $|\hat{\phi}_{\exp}(\omega, r_1)|$ and $|\hat{\phi}_{\exp}(\omega, r_2)|$ denote experimentally determined amplitude spectra for r_1 and r_2, respectively. It is significant that the procedure proposed for determining $\beta(\omega)$ requires neither information about the real distribution of recoil pressure momentum $\Pi(r)$, nor absolute measurements of observation angles.

In addition to the determination of attenuation spectrum, there exists the possibility of reconstructing the recoil momentum distribution $\Pi(R)$ and, hence, to verify the assumptions on the $\Pi(R)$ dependence stated in §2. (To avoid ambiguity, here R stands for the momentum surface distribution variable while r will denote the distance to the observation point in the surface plane.) The reconstruction is regarded to be of importance to understand the phenomena following the interaction of laser radiation

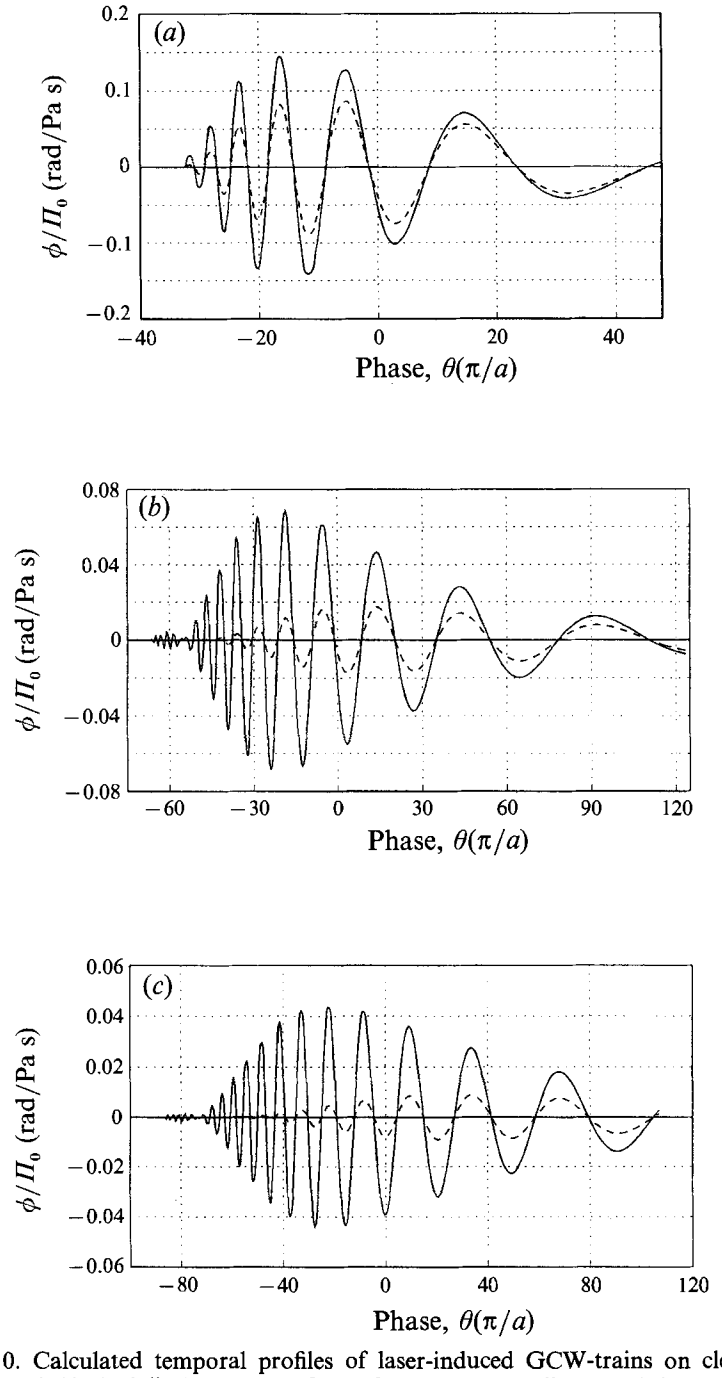

FIGURE 10. Calculated temporal profiles of laser-induced GCW-trains on clean (solid line) and contaminated (dashed line) water surfaces. Impact spot radius $a = 1.6$ mm. (*a*) $r = 35$ mm; (*b*) $r = 60$ mm; (*c*) $r = 80$ mm.

with liquids. The function $\Pi^*(R)$ (the asterisk implies the experimental counterpart of the real distribution $\Pi(R)$) can be determined by applying the inverse Fourier–Bessel transform to the dependence $\hat{\Pi}(k)$, which in turn can be found from (39):

$$\Pi^*(R) = \tfrac{1}{2}\rho_0 \left(\frac{r}{2\pi}\right)^{\frac{1}{2}} \int_0^\infty k^{-\frac{3}{2}}(\omega)\, J_0(k(\omega)\, R)\, \mathrm{e}^{\frac{\beta(\omega)}{U(\omega)} r}\, \omega |\phi_{\exp}(\omega, r)| \mathrm{d}\omega. \tag{41}$$

In (41) the integration variable k is substituted by ω according to $\omega = \Omega(k)$. To reconstruct the distribution $\Pi(R)$ one should take a clean liquid with an exactly known attenuation spectrum: $\beta(\omega) = -2\nu k^2(\omega)$, though the real spectrum $\beta(\omega)$ could also be measured directly. Formula (41) is valid only for the case of axial symmetry of the $\Pi(R)$ function. Besides, the theory of Fourier–Bessel transforms implies that the distribution $\Pi(R)$ is a function of limited variation near the point R. The extent of correspondence between the actual distribution $\Pi(R)$ and its experimental counterpart $\Pi^*(R)$ depends upon the accuracy of the asymptotic expression (39) and, mainly, upon the accuracy of measurements of GCW-train spectra, $\hat{\phi}_{\exp}$. In practice, reliable determination of $\hat{\phi}_{\exp}$ is possible in some limited frequency band $\Delta\omega$ which is determined by the quality of the experimental set-up. Upper and lower boundaries of the band for a given observation point could be found, for example, from the condition that the signal/noise ratio be equal to unity for a particular spectrum component of a GCW-packet. When the frequency band $\Delta\omega$ (or the band Δk) is given, the spatial resolution of the distribution $\Pi^*(R)$ reconstruction is approximately determined by

$$\delta R \approx 1/\Delta k.$$

The smaller details of the distribution will be lost and the function $\Pi^*(R)$ will in any case be smoother than the actual distribution $\Pi(R)$. So, the best accuracy of reconstruction may be reached when the nearest observation point r satisfying the conditions of the derivation of (39) is chosen. For that distance the attenuation of the high-frequency components is comparatively small and the maximum upper frequency limit of $\Delta\omega$ may be obtained. The experimental realization of the technique in question is considered in the next subsection.

4.2. *Experimental investigation*

4.2.1. *Experimental set-up and measurement procedure*

The method of dynamic diagnostics of the air–liquid interface based on the analysis of laser-induced GCW-trains was realized in the experiment represented schematically in figure 11. The distinctive feature of the proposed variant of GCW-diagnostics is the remote, contactless generation and detection of GCW-trains.

The radiation of a discharge pulsed CO_2- laser was used to induce GCWs. The radiation energy was controlled by means of a nichrome wire differential bolometer. The surface waves were generated in a liquid-filled quartz cuvette which was carefully cleaned by acetone. The GCW detection was carried out by surface reflection of the continuous radiation from the probe He-Ne laser. The probe laser beam was expanded to a large diameter (≈ 10 cm) and then focused onto the liquid surface. The convergency angle was $\approx 25°$. The light spot diameter on the surface was determined by the quality of the optical elements instead of the diffraction limit and was equal to $d \approx 0.2$ mm. As the radii of surface curvature during the propagation of a GCW with wavelengths $\lambda \geqslant 2$ mm are much greater than the diameter d, the detection of the reflected probe beam enables the reconstruction of the inclination angle at any point of the GCW-profile without distortions. Let us consider the angle detection scheme in

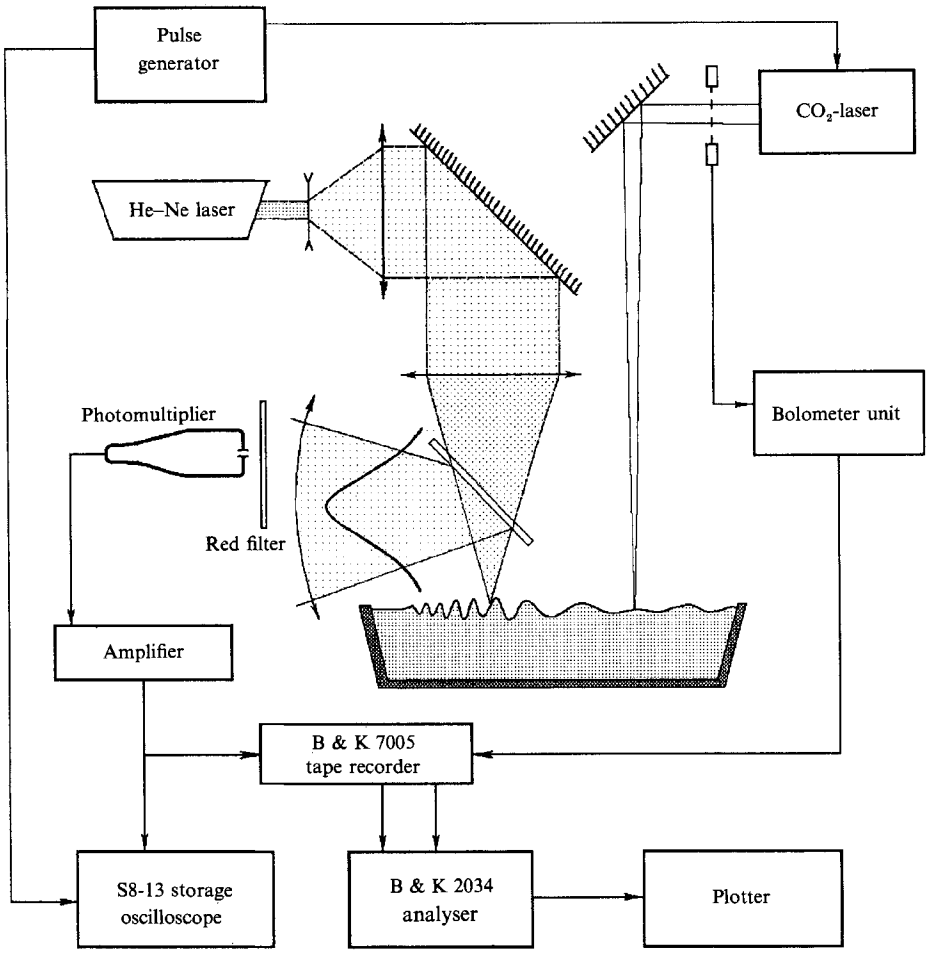

FIGURE 11. Experimental set-up for remote generation and detection of GCWs on a liquid–air interface.

more detail. The intensity distribution across the probe beam was found to be Gaussian with fair accuracy. The optical scheme was adjusted so that the centre of the Gaussian intensity distribution wing of the laser beam reflected from an undisturbed surface ($\phi = 0°$) was situated precisely on the narrow input aperture of a photomultiplier, as displayed in figure 11. The declination of the laser beam due to the surface displacements resulted in a photomultiplier output signal modulation $-\Delta i/i_0$ (i_0 is the average current of the photomultiplier output). The linearity of the dependence $\Delta i/i_0(\phi)$ and the range of inclination angles that could be measured were evaluated in the following calibration experiment. At the point where the probe laser beam spot had to be located on the liquid surface after filling of the cuvette, a small (1.5×1.5 mm) mirror attached to a nichrome wire was situated (this attachment had been the key element of an obsolete ballistic galvanometer). Under the action of a sinusoidal voltage applied to an electromagnetic coil the wire was twisted and the mirror oscillated. For small oscillation amplitude the photomultiplier signal had a precisely sinusoidal shape. This is because any small fragment of a Gaussoid wing may be approximated by a linear law and for small probe beam declination angles the shape of the electric signal must coincide with the surface inclination angle variations. In the experiment the

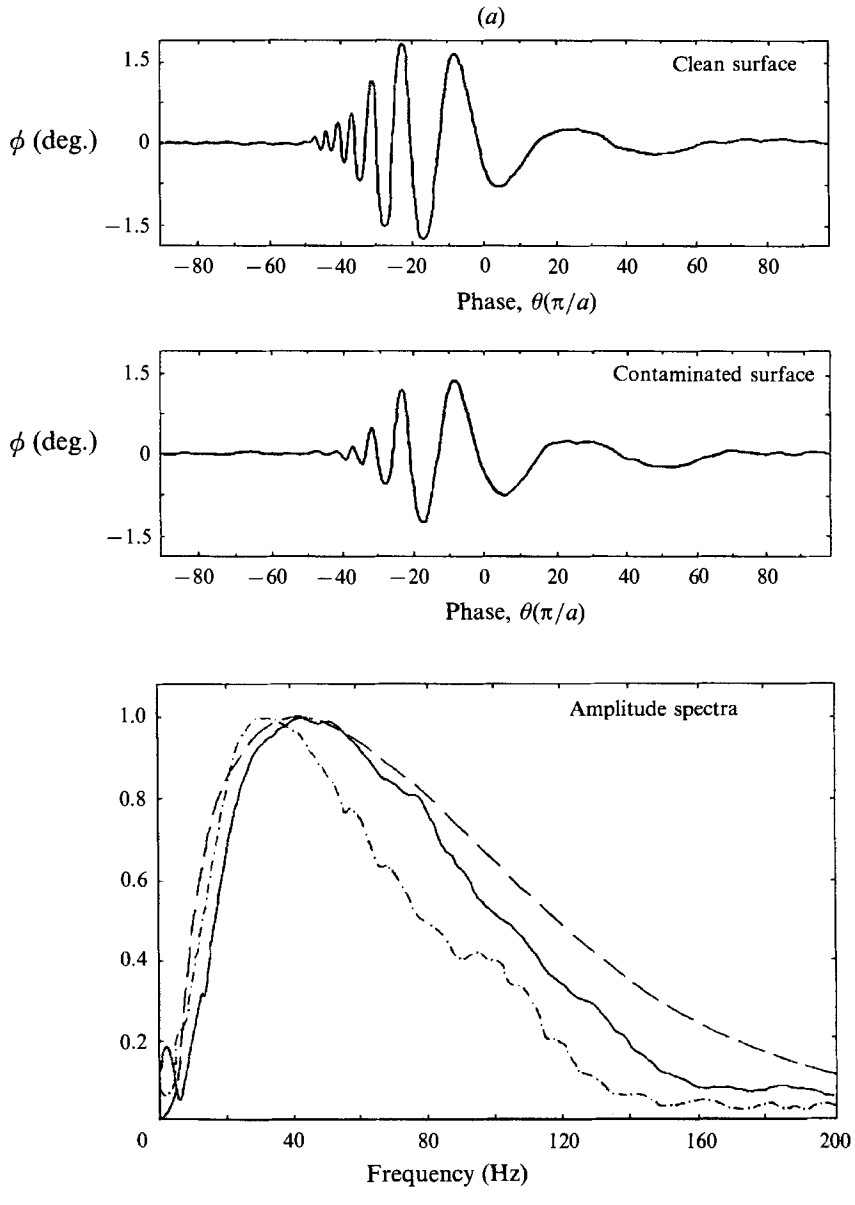

FIGURE 12(*a*). For caption see p. 411.

linearity of the dependence $\Delta i(\phi)$ was found to hold in the range of angles $\pm 3.5°$. Larger-amplitude oscillations were followed by some distortions of the sinusoidal shape of the signal. As the intensity distribution was measured immediately in the plane of the photomultiplier aperture, these distortions could be accounted for in the digital processing of output signals.

The high-sensitive photomultiplier output signal, after amplification, was recorded in one of the channels of a B&K-7005 tape recorder. The second channel was used to register the signal from the bolometer. Thus, the laser energy was controlled and the time delay between GCW generation and detection was measured. The permanent on-line monitoring of GCW-train profiles was carried out by means of a storage

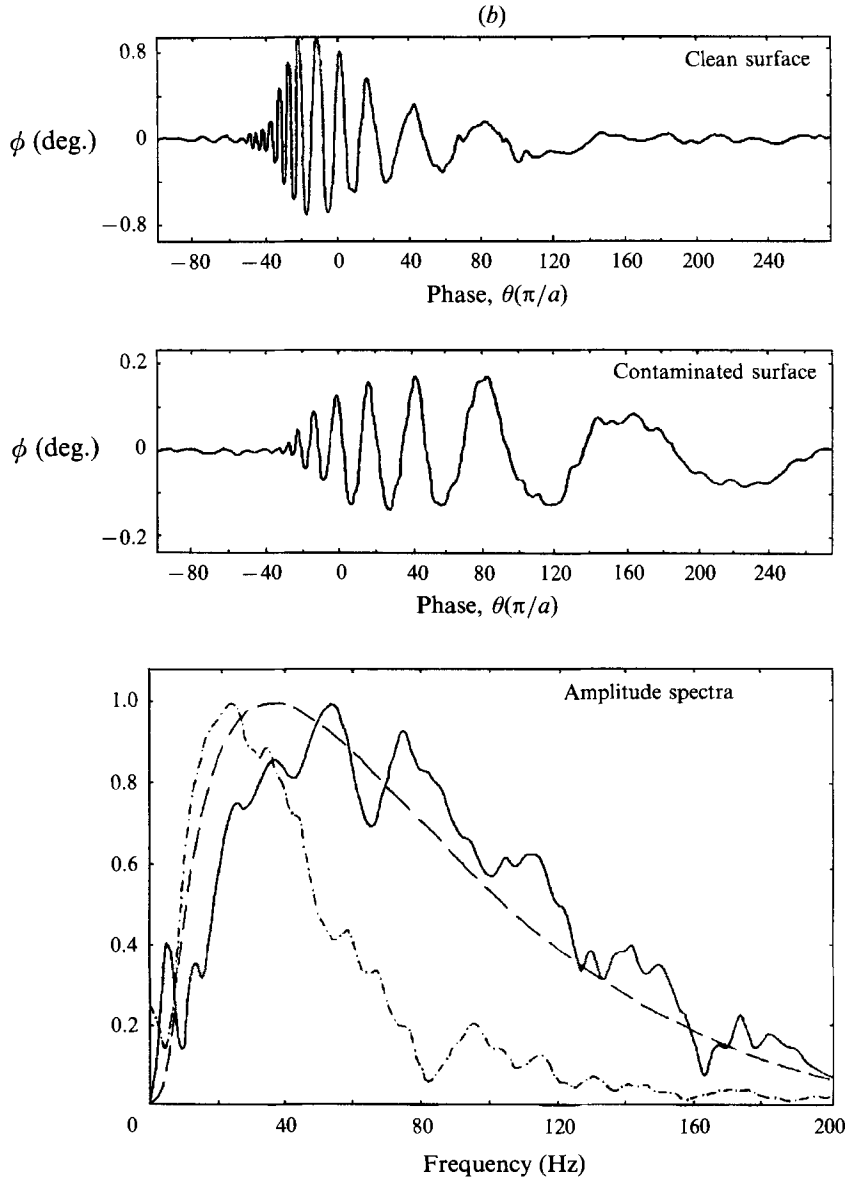

FIGURE 12(*b*). For caption see facing page.

oscilloscope. To minimize the effect of micro-vibrations of the laboratory desk plate on the measurements and the influence of uncorrelated electric noise, averaging over 100 realizations was performed. The technique gave an accuracy of the inclination angle measurements of about 0.05°. The CO_2-laser shock was driven by a random signal generator (*hp*-7422A) with a repetition rate of 5–7 s (this time was needed to let the liquid surface become quiescent). The averaging and digital processing of the signals were carried out by the two-channel analyser B & K-2034.

The liquid under investigation was purified twice-distilled water. After each series of measurements (normally comprising recordings at one observation point) the surface layer was flushed over the cuvette brim to eliminate the effect of the time-dependent

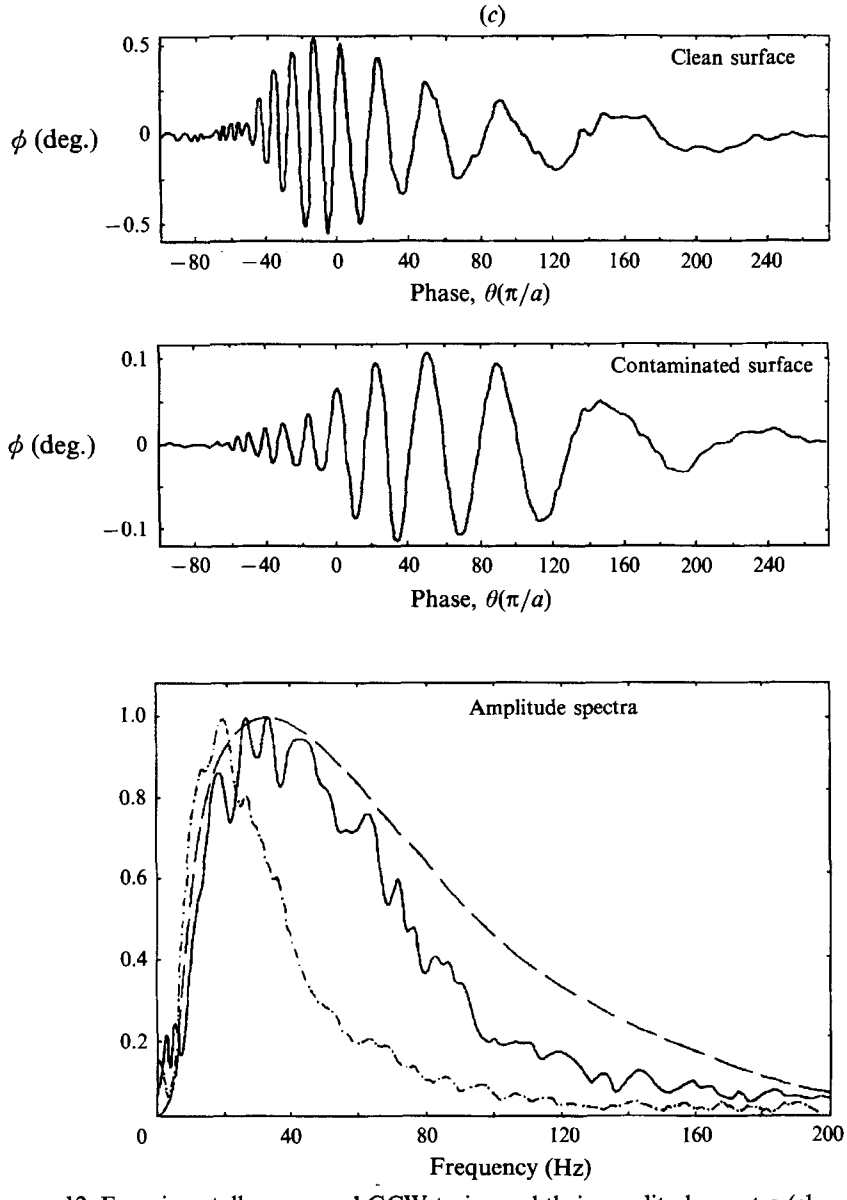

FIGURE 12. Experimentally measured GCW-trains and their amplitude spectra (clean surface (——), theory for clean surface (– – –), contaminated surface (–·–·–)) for three observation points: (*a*) $r = 35$ mm; (*b*) $r = 60$ mm; (*c*) $r = 80$ mm. Impact spot radius $a \approx 1.6$ mm. Surfactant concentration 15 mg/m^2.

'dirtiness' of the surface described earlier by McGoldrik (1970). To investigate the influence of surface contamination on the GCW propagation a diesel oil film was deposited onto the surface by means of a measuring pipette. The surface contamination concentration was varied in the range 10–30 mg/m^2. The other physical–chemical parameters of the dirty surface were not controlled, so only a qualitative comparison of measured spectra $\beta(\omega)$ with theoretical ones is relevant.

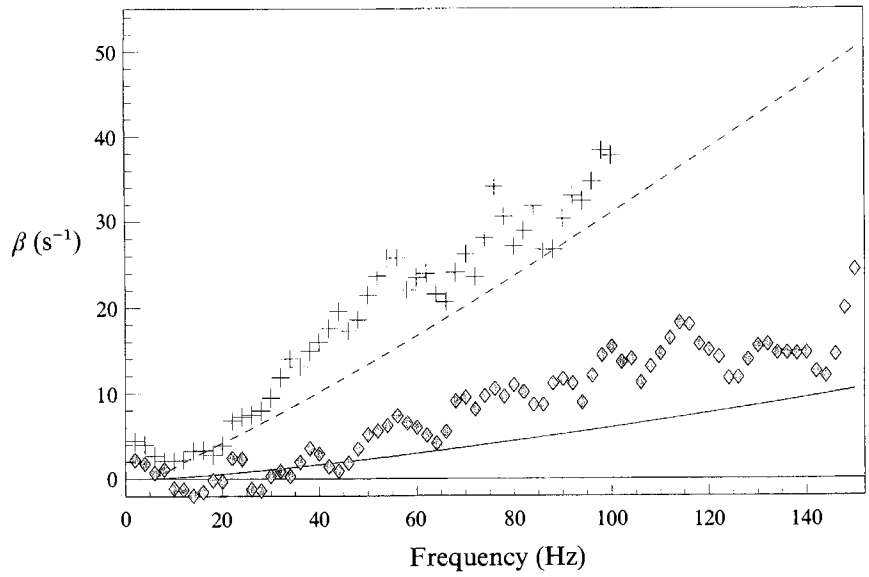

FIGURE 13. Experimentally reconstructed GCW-attenuation spectrum for clean (◇) and contaminated (+) water surfaces. The solid curve corresponds to the theoretical dependence $\beta = 2\nu k^2$ for clean surfaces and the dashed line is calculated for film-covered surfaces with dilational modulus $\epsilon = 7 \times 10^{-3}$ N/m.

4.2.2. *Results*

In figure 12(*a–c*) experimentally recorded GCW-trains and their amplitude spectra on clean and contaminated water surfaces are presented for three observation point distances from the pressure impact spot. The laser energy density in these experiments was equal to $w \approx 1.6$ J/cm^2. In accordance with absolute measurements reported in §2 this corresponds to the recoil pressure momentum $\Pi_0 \approx 0.2$ Pa s. It is noteworthy that the measured profiles are in good agreement with those calculated using the expressions from linear theory (see figure 10). Some discrepancy appears only for the leading, high-frequency part of a GCW-packet. The reason is that the surface is never ideally clean and, hence, high-frequency components are damped faster than given by the theoretical expressions for a pure liquid surface. This follows from the comparison of the experimentally measured spectra and the theoretical ones calculated for pure water.

The laser-induced GCW-train spectra measurements enabled the attenuation spectrum $\beta(\omega)$ to be obtained according to (40). The reconstruction was carried out by using the spectra measured at observation points $r = 60$ and 80 mm. The experimental determination of $\beta(\omega)$ was influenced by the errors of the GCW-spectra measurements, especially in the frequency intervals where the absolute values of $\hat{\phi}_{\exp}(\omega, r)$ are low. So, the most accurate reconstruction of $\beta(\omega)$ is possible over the frequency range agreeing with the maximum values of $\hat{\phi}_{\exp}(\omega, r)$. Given the particular frequency band of interest (for example, when a relaxation process with definite time constant is under investigation), the exciting laser spot size should be adjusted properly.

The results of the $\beta(\omega)$ reconstruction for the spot radius $a \approx 1.6$ mm are represented in figure 13. Also displayed are the theoretical curves for pure and contaminated water surfaces. The surface dilational modulus $\epsilon \approx 7 \times 10^{-3}$ N/m for the film-covered surface is chosen to provide the best agreement with the experimental data. It can be seen from figure 13 that the real air–liquid interface is always slightly contaminated and the

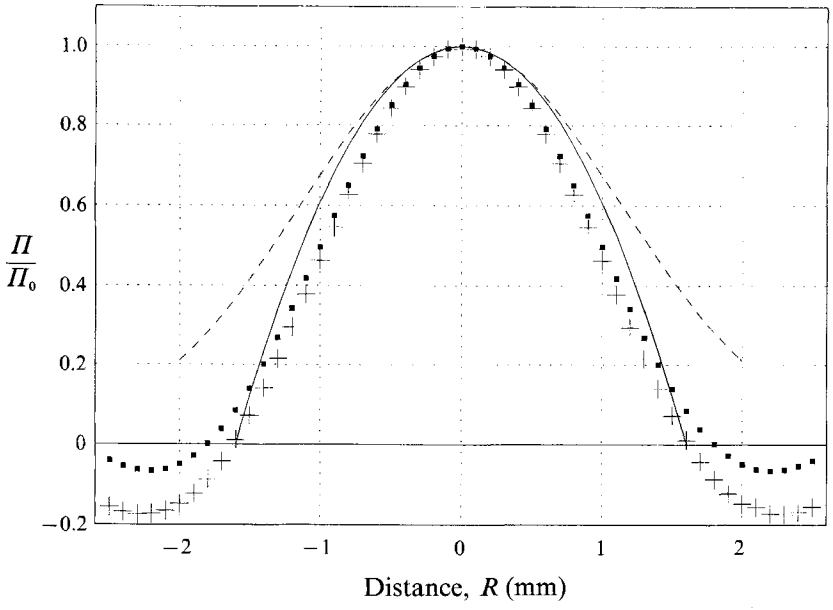

FIGURE 14. Reconstruction of recoil pressure momentum distribution with the amplitude spectra measured in two observation points: $r = 60$ mm (+) and $r = 80$ mm (■). The solid curve represents the parabolic law of the $\Pi(R)$ distribution adopted in theoretical calculations and the dashed curve represents a Gaussian distribution of laser intensity.

attenuation of GCWs is a very sensitive instrument to evaluate the contamination. The accuracy of reconstruction for low (< 10 Hz) and high (> 100 Hz) frequencies is insufficient, as the high-level frequency components for the radius chosen are in the range 20–70 Hz.

A dramatic increase of the measurement accuracy and the efficiency of complex interface investigations may be obtained by narrowing and subsequent tuning the frequency band of GCW-trains. This unique possibility of controlling the frequency band is given by the method of GCW generation itself. By placing ring-shaped masks across the laser beam path one can form the desired recoil momentum distribution $\Pi(R)$ and therefore the appropriate frequency structure of the GCW-train.

The problem of the reconstruction of the actual distribution $\Pi(R)$ is important for the theory of the interaction of powerful laser radiation with liquids. The reconstructed distribution $\Pi^*(R)$ was determined by digital processing of amplitude spectra measured for clean water (the observation points were at $r = 60$ and 80 mm) in accordance with formula (41). The results of the reconstruction are presented in figure 14. Here the parabolic distribution $\Pi(R) \sim (1-(R/a)^2)$ used in the theoretical simulations and the Gaussian distribution of laser intensity $I(R) \sim \exp(-R^2/a^2)$ are also displayed for comparison. The agreement between theoretically proposed and reconstructed distributions proved to be good enough to validate the assumptions stated in §2. It is worth noting that the attenuation spectrum $\beta(\omega)$ taken for the processing was a directly measured one on a real surface instead of a theoretically calculated one. The width of the GCW-spectrum at the observation points $r = 60$ and 80 mm does not vary appreciably, so in both cases the spatial resolution of the reconstruction is considered to be the same: $\delta R \approx 0.1$ mm.

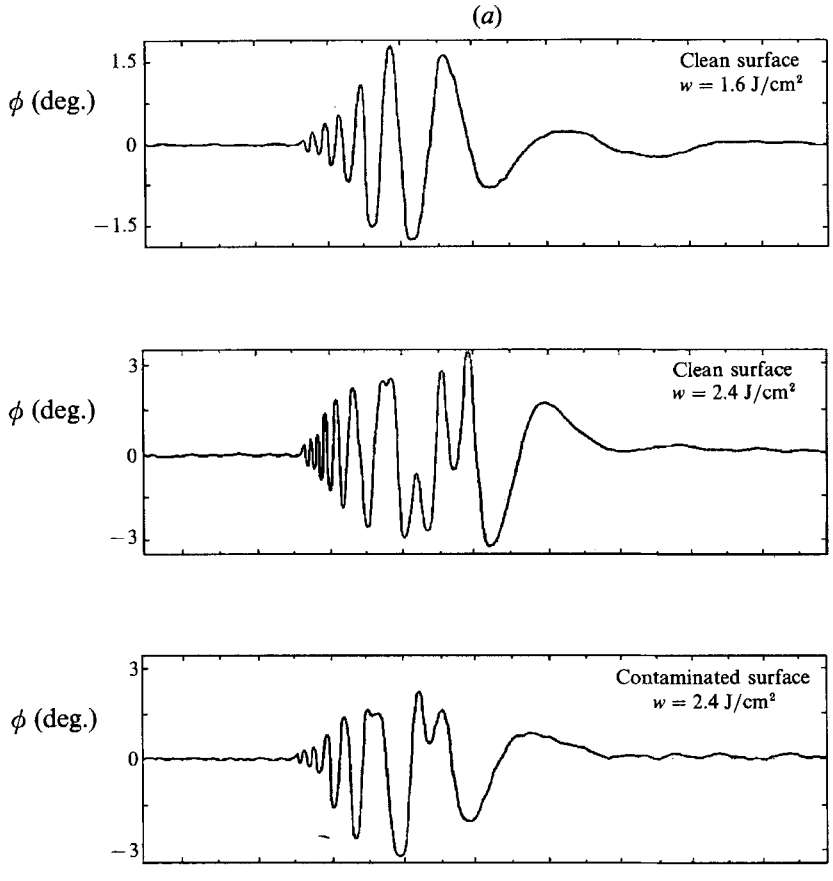

FIGURE 15(*a*). For caption see facing page.

5. Nonlinear evolution of GCW packets

Nonlinear interactions of waves on a free liquid surface have been examined by many authors. For example, the conditions for triplet resonance interactions in GCW-packets were studied theoretically by McGoldrick (1965) and later also experimentally by McGoldrick (1970). Effective collinear interaction in narrowband GCW-packets is possible only near the distinct frequency $f_0 = 9.8$ Hz for which the generation of second harmonics with phase velocity equal to that of the main wave is observed. For frequencies near that of the gravitational part of the spectrum $f \leqslant f_0$ the nonlinearity leads to sharpening of crests of sinusoidal waves and smoothing of hollows (Stokes profile), and for the capillary part of the spectrum $f \geqslant f_0$ the crests are smoothed and the hollows are sharpened (Crapper profile). Corresponding sinusoidal profile distortions were observed by McGoldrick (1970). It is important to mention one more type of resonant interaction which was described in the fundamental work of Djordjevich & Redekopp (1977). They theoretically revealed resonance for narrowband high-frequency capillary wavetrains which corresponds to a long wave/short wave interaction when the group velocity of the short (capillary) wave matches the phase velocity of the long (gravity) wave on shallow water $C_{\mathrm{ph}} = (\mathrm{gH})^{\frac{1}{2}}$ (H is the depth of the liquid). In that work, plots to determine the packet stability/instability regions with

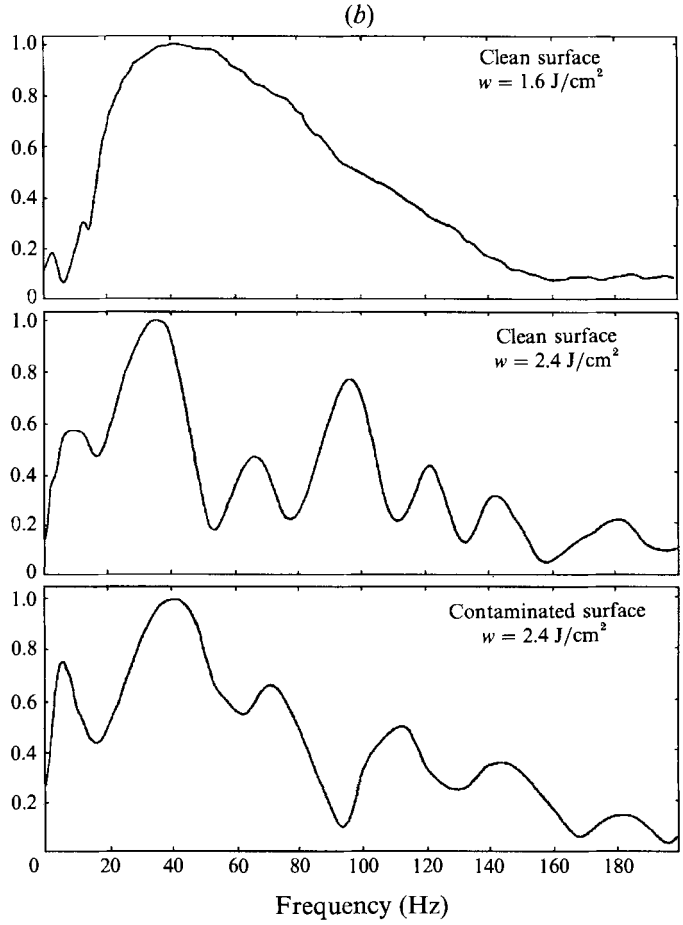

FIGURE 15. (*a*) Nonlinear evolution of GCW-train profile with increase of laser energy; (*b*) the corresponding amplitude spectra. Impact spot radius $a \approx 1.6$ mm. $r = 35$ mm.

respect to the fluid depth, its density and surface tension were presented. It should be noted that almost all theoretical and experimental results obtained till now concern the narrowband, quasi-monochromatic packets for which perturbation theory in the slowly varying amplitude approximation may be applied and second-order nonlinear interactions may be traced. The nonlinear evolution of broadband surface disturbances has been comparatively poorly investigated. Therefore, the experimental data on the generation of nonlinear GCW-packets by means of laser radiation that will be reported below are thought to be of interest.

Experimental data presented in table 1 reveal the range of laser intensities corresponding to linear surface waves to be rather small. So, in the experiment the increase of threshold energy density w_{thr} by 50% led to nonlinear distortions of GCW-profiles. The features of our experimental set-up enabled us to measure the inclination angles without distortion in the range $\pm 3.5°$, hence only weakly nonlinear GCWs were investigated.

The measurements were carried out with the experimental arrangement described in the previous section. For every observation point, besides linear GCW-profiles corresponding to $w \approx 1.6$ J/cm^2, the GCW-packets for $w \approx 2.4$ J/cm^2 were also recorded first on a clean water surface and then on a film-covered surface. Furthermore,

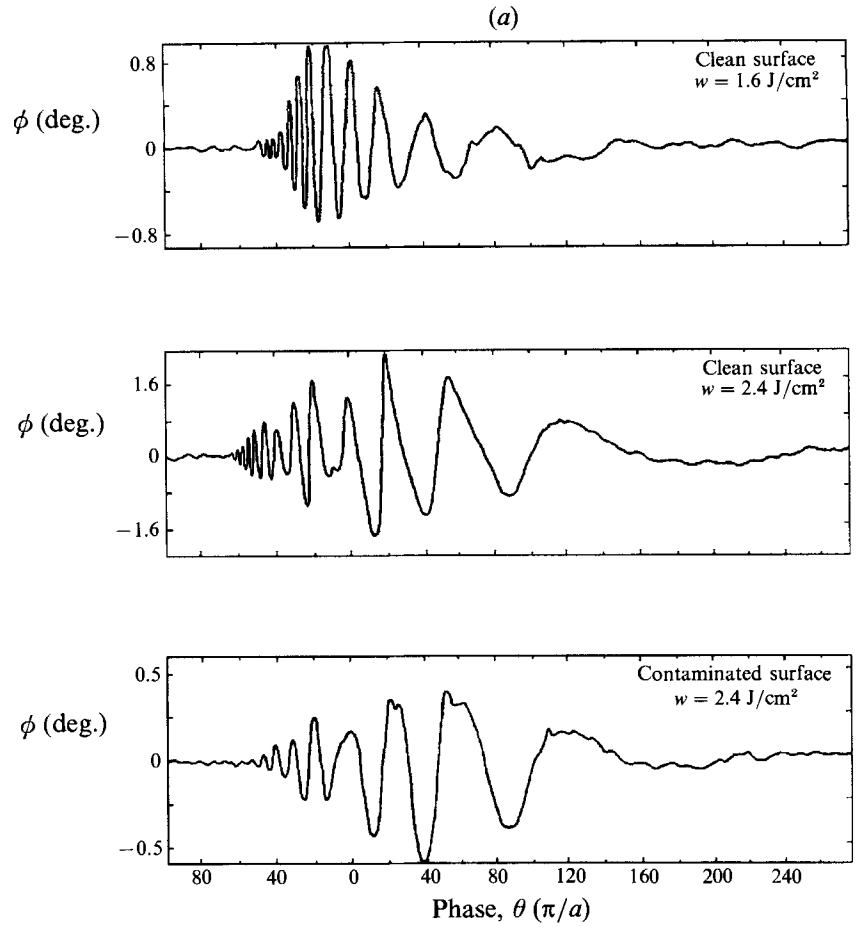

FIGURE 16(a). For caption see facing page.

for $r = 80$ mm it turned out to be meaningful to include an intermediate profile for the energy density value $w \approx 1.9$ J/cm² which enabled us to trace the successive transformation of GCW-profiles with laser energy increase. Experimental data obtained are presented in figure 15,16 and 17. Here the amplitude spectra of GCW-packets are also displayed to elucidate the nonlinear interaction-induced energy redistribution in the frequency spectrum.

Analysis of experimental data leads to some interesting conclusions. First of all, from figures 15–17 it follows that the energy density value $w \approx 1.6$ J/cm² may be considered as a linearity threshold. Exceeding this value results in nonlinear distortions of GCW-profiles. Indeed, given the quantitative relation between the amplitude ϕ_0 of the inclination angles and the amplitude Π_0 of the pressure recoil momentum distribution according to the linear theory (33), the energy density $w \approx 1.6$ J/cm² was found to correspond to a momentum amplitude $\Pi_0 \approx 0.2$ Pa s. The condition of linear approximation (7) for $a = 1.6$ mm claims $\Pi_0 \ll (a\sigma\rho_0)^{\frac{1}{2}} \approx 0.35$ Pa s, so the value $w \approx 1.6$ J/cm² may be really considered as a threshold. For $w \approx 2.4$ J/cm² the surface peak displacement from equilibrium h_0 is greater than a (the displacement $h_0 \approx a$ corresponds to $w \approx 2.1$ J/cm²), though the rapid hemisphere-like expansion regime with bubble formation has not yet developed. In this sense the nonlinearity concerned

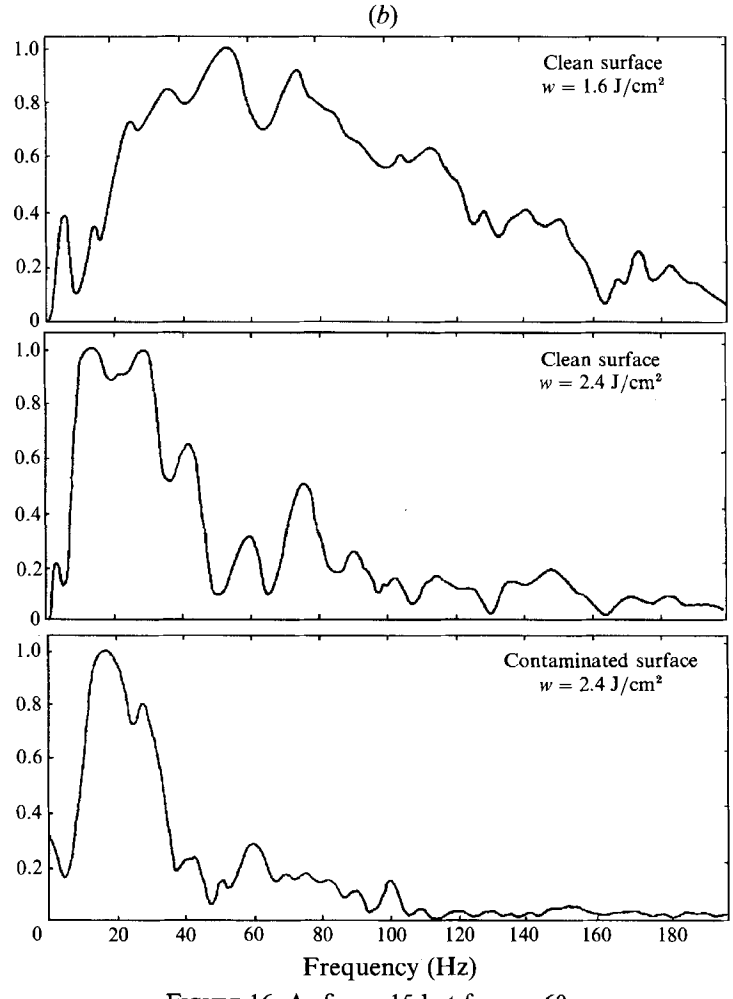

FIGURE 16. As figure 15 but for $r = 60$ mm.

may be considered 'weak'. One more noteworthy result consists in the fact that for nonlinear GCW-profiles at all observation distances (for a clean surface) the quadratic dependence $\phi_0 \sim w^2$ holds accurately in the whole range of laser intensities under study. Therefore, the second-order nonlinearity holds. In this connection it is relevant to mention the possible nonlinear interaction mechanism. It follows from amplitude spectra that spectral components for frequencies of about 10 Hz for which the collinear triplet resonance interaction is most effective are not of appreciable amplitude in our particular case. Besides, the shape of the amplitude spectra does not match the mechanism for resonance harmonic generation. On the other hand, it should be noted from the GCW-packet evolution with distance for $w \approx 2.4$ J/cm^2, that the initial packet ejects another, much higher-frequency packet, which passes the initial one while propagating. Furthermore, in figure 17(*a*) one can observe the decay of the initial packet to three nearly isolated packets. The quantitative estimation we made suggests the following explanation for the effect in question. In this particular case a resonance mechanism analogous to that reported by Djordjevich & Redekopp (1977) can be referred to. The group of low-frequency waves spreading out with group velocity $U(k_{\mathrm{low}})$ effectively interacts with high-frequency components of the packet which have

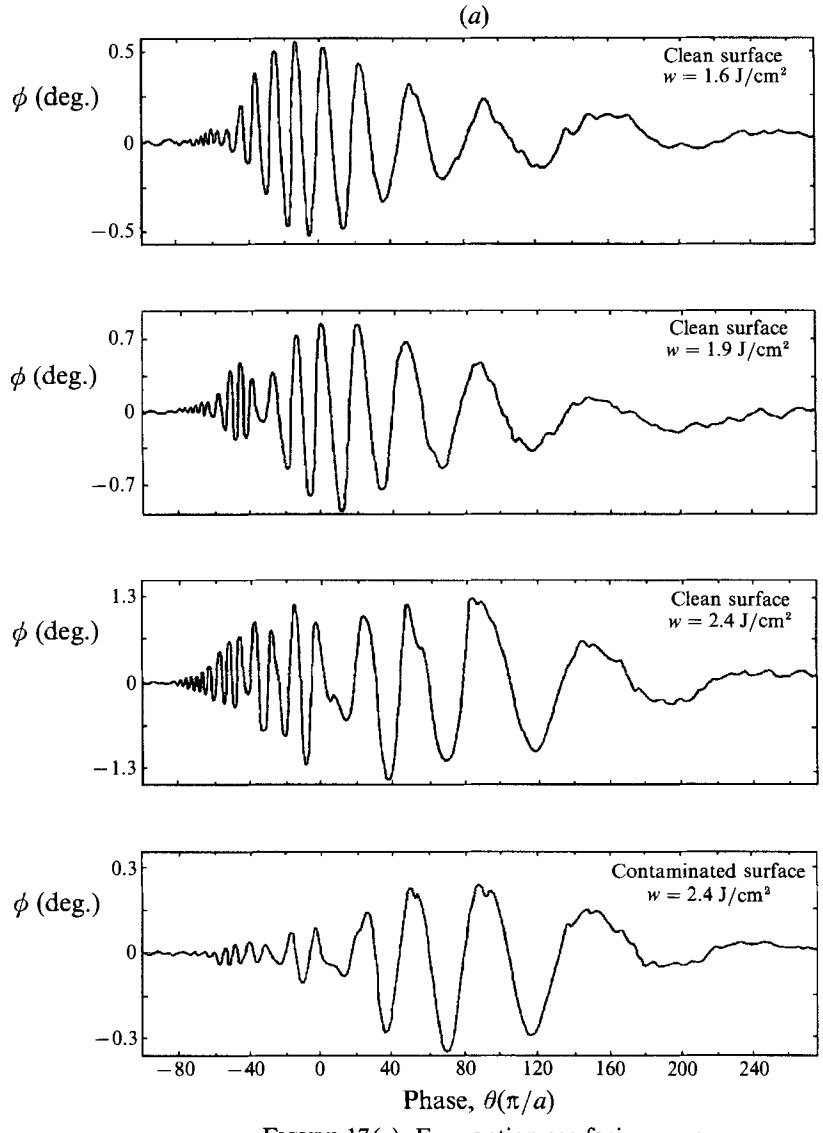

FIGURE 17(*a*). For caption see facing page.

a phase velocity $C_{\mathrm{ph}}(k_{\mathrm{high}})$ coincident with $U(k_{\mathrm{low}})$. The interaction is possible essentially due to the broadband nature of the initial disturbance. By separating, owing to dispersion, from the main packet the high-frequency component group forms a new packet with group velocity much higher than that of the initial packet, so the new packet gradually runs away from the 'mother' packet. A schematic of the interaction is displayed in figure 18, where the frequency values matching two maxima of the amplitude spectrum for $r = 35$ mm are marked. For larger distances the dispersion and attenuation have to be taken into account to obtain the relation between the carrier frequencies of the packets induced. By the way, in our case the attenuation due to contamination of the surface does not violate substantially the nonlinear interaction pattern – its influence is reduced to the faster attenuation of high-frequency spectrum components induced by the interaction. Indeed, the attenuation length, which can be evaluated by using experimental data for the $\beta(\omega)$ dependence (see figure 13) for near

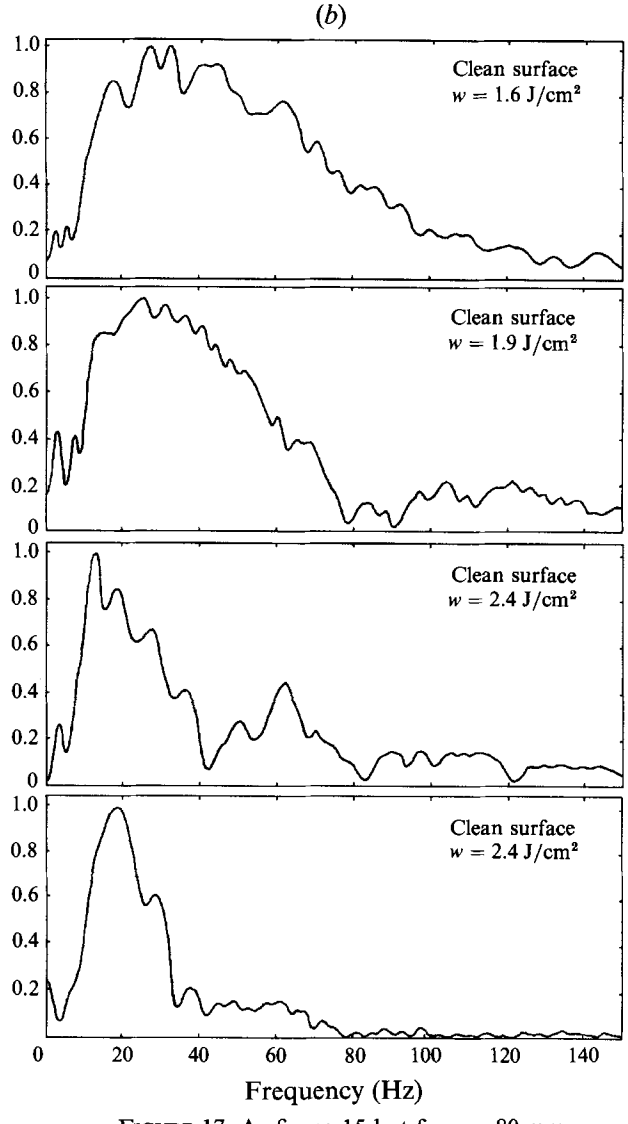

FIGURE 17. As figure 15 but for $r = 80$ mm.

maximum frequencies of 20–40 Hz, lies in the range 3.5–6 cm. Though the experimental data presented in figures 15–17 show that by distance the $r = 35$ mm the nonlinear transformation has already occurred, the inclination angles are sufficiently small and the further evolution of the packet is reduced to dispersion-driven packet deformation.

6. Conclusions

Hydrodynamic phenomena resulting from the interaction of pulsed laser radiation with highly absorbing dielectric fluids are considered to be of interest for several reasons.

First, the interaction in question allows the transfer to the fluid of a recoil pressure momentum of almost any desired amplitude and spatial distribution. This in turn gives rise to the generation of wide-range surface disturbances. The investigation of these

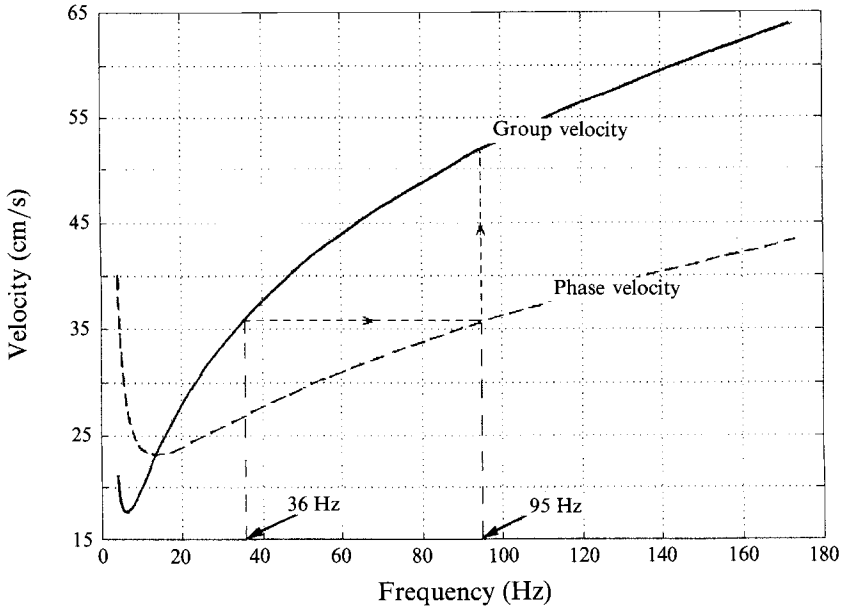

FIGURE 18. A qualitative scheme of the nonlinear interaction for broadband GCW-packets. The arrows mark the mode of precursor packet formation.

disturbances on the one hand gives an opportunity to obtain additional information about the features of the interaction (in particular, to reconstruct the value and surface distribution of recoil pressure momentum transferred to the surface and therefore to find the energy of liquid motion and the coefficient of transformation of laser energy to hydrodynamic energy), and, on the other hand, the disturbances can be used as standard test signals to probe the interface properties. Furthermore, the remote mode of the laser-induced GCW-based analytical procedure and also the possibility to control the spectral characteristics of GCWs are useful distinctive features of the proposed method compared to the existing technique of physical–chemical analysis of interfaces.

Lastly, there is the unique possibility of tracing experimentally the nonlinear evolution of broadband wave packets in dispersive media with attenuation. Flexible adjustment of the amplitude and spectrum of finite amplitude GCW-packets is expected to provide a useful experimental tool for promoting theoretical investigations of nonlinear interactions in broadband surface disturbances.

We hope that further experiments let us fully realize the potential advantages of laser-induced GCW usage following from the results reported here.

REFERENCES

ALEKSEEV, V. N., EGEREV, S. V., NAUGOL'NYKH, K. A., OVCHINNIKOV, O. B., PASHIN, A. E. & PUCHENKOV O. V. 1987 Acoustic diagnostics of transient interaction processes between optical radiation and a highly absorbing dielectric liquid. *Sov. Phys. Acoust.* **33**, 561–565.

BATCHELOR, G. K. 1967 *An Introduction to Fluid Dynamics*. Cambridge University Press.

BELL, C. E. & MCCABEE, B. S. 1974 Shock wave generation in air and in water by CO_2-TEA laser radiation. *Appl. Optics*, 605–615.

BUNKIN, F. V. & TRIBEL'SKII, M. I. 1980 Nonresonant interaction of powerful optical radiation with a liquid. *Sov. Phys. Usp.* **23**, 193–240.

DERIBAS, A. A. & POHOZHAEV, S. I. 1962 On a problem of very intense explosion on liquid surface. *Dokl. Akad. Nauk SSSR* **144**, 524–527.

DOMMERMUTH, D. G. & YUE, D. K. P. 1987 Numerical simulation of nonlinear axisymmetric flows with a free surface. *J. Fluid Mech.* **178**, 195–219.

DJORDJEVIC, V. D. & REDEKOPP, L. G. 1977 On two-dimensional packets of capillary–gravity waves. *J. Fluid Mech.* **79**, 703–714.

EGEREV, S. V., LYAMSHEV, L. M. & PUCHENKOV, O. V. 1990 Laser dynamic optoacoustic diagnostics of condensed media. *Sov. Phys. Usp.* **160**, 739–762.

EMMONY, D. C. 1985 Interaction of IR-radiation with liquids. *Infrared Phys.* **25**, 133–139.

EMMONY, D. C., GEERKEN, B. M. & STRAAIJER, A. 1976 The interaction of 10.6 μm laser radiation with liquids. *Infrared Phys.* **16**, 87–92.

KOLOMENSKII, A. A. 1986 Excitation of surface waves in compressible fluid by volume sources. *Pis'ma Zh. Tekhn. Fiz.* **12**, 244–248.

LAMB, H. 1932 *Hydrodynamics*. Cambridge University Press.

LANDAU, L. D. & LIFSHITZ, E. M. 1986 *Hydrodynamics*. Moscow: Nauka.

LE MEHAUTE, B. 1988 Gravity–capillary rings generated by water drops. *J. Fluid Mech.* **197**, 415–427.

LEVICH, V. G. 1962 *Physicochemical Hydrodynamics*. Prentice Hall.

LUCASSEN-REYNDERS, E. H. & LUCASSEN, J. 1970 Properties of capillary waves *Adv. Colloid Interface Sci.* **2**, 347–395.

MCGOLDRICK, L. F. 1965 Resonant interactions among capillary–gravity waves. *J. Fluid Mech.* **21**, 305–331.

MCGOLDRICK, L. F. 1970 An experiment on second-order capillary-gravity resonant wave interactions. *J. Fluid Mech.* **40**, 251–271.

MININ, V. F. 1964 On explosion on a liquid surface. *Zh. Prikl. Mekh. Tekhn. Fiz.* N3, 159–161.

OGUZ, H. N. & PROSPERETTI, A. 1990 Bubble entrainment by the impact of drops on liquid surfaces. *J. Fluid Mech.* **219**, 143–179.

PUCHENKOV, O. V. & PASHIN, A. E. 1989 Remote probing of liquid surface by laser induced gravity-capillary waves. In *Proc. All-Union Seminar on Photoacoustic spectroscopy and microscopy, Dushanbe*, p. 45–46 (in Russian).

SEDOV, L. I. 1946 Air motion induced by very intense explosion. *Dokl. Akad. Nauk SSSR* **52**, 17–20.

VAN DEN TEMPEL, M. & LUCASSEN-REYNDERS, E. H. 1983 Relaxation processes at fluid interfaces. *Adv. Colloid Interface Sci.* **18**, 281–301.

VITSHAS, A. F., KORNEEV, V. V. & MENAKHIN, L. P. 1987 Recoil momentum under non-steady-state surface evaporation of water. *Tekhn. Vysokikh Temp.* **25**, 312–317.

WORTHINGTON, A. M. & COLE, M. A. 1897 Impact with a liquid surface studied by the aid of instantaneous photography. *Phil. Trans. R. Soc. Lond.* A **189**, 137–151.

ZOSIMOV, V. V., KUKUSHKIN, M. U., NAUGOL'NYKH, K. A. & PUCHENKOV, O. V. 1989 Hydrodynamic phenomena in the interaction of powerful laser radiation with highly absorbing dielectric liquid. *Zh. Prikl. Mekh. Tekhn. Fiz.* N5, 33–41.